nature nanotechnology

Article

https://doi.org/10.1038/s41565-023-01394-3

Hierarchical helical carbon nanotube fibre as a bone-integrating anterior cruciate ligament replacement

Received: 18 April 2022

Accepted: 31 March 2023

Published online: 4 May 2023

Check for updates

Liyuan Wang[1,7], Fang Wan[2,7], Yifan Xu[1,7], Songlin Xie[1,7], Tiancheng Zhao[1,7], Fan Zhang[3,7], Han Yang[1], Jiajun Zhu[3], Jingming Gao[1], Xiang Shi[1], Chuang Wang[1], Linwei Lu[4], Yifan Yang[5], Xiaoye Yu[1], Shiyi Chen[2] ✉, Xuemei Sun[1] ✉, Jiandong Ding[1], Peining Chen[1] ✉, Chen Ding[3] ✉, Fan Xu[5], Hongbo Yu[6] & Huisheng Peng[1] ✉

High rates of ligament damage require replacements; however, current synthetic materials have issues with bone integration leading to implant failure. Here we introduce an artificial ligament that has the required mechanical properties and can integrate with the host bone and restore movement in animals. The ligament is assembled from aligned carbon nanotubes formed into hierarchical helical fibres bearing nanometre and micrometre channels. Osseointegration of the artificial ligament is observed in an anterior cruciate ligament replacement model where clinical polymer controls showed bone resorption. A higher pull-out force is found after a 13-week implantation in rabbit and ovine models, and animals can run and jump normally. The long-term safety of the artificial ligament is demonstrated, and the pathways involved in integration are studied.

Ligaments and tendons are made up of fibrous connective tissues and are vital for joint movement and stability[1–4]. Ligaments link bones together whereas tendons connect muscle to bone. Because these tissues transmit high tensile forces, they must be strong, flexible and stable[3,5–7]. Native ligaments composed of organic molecules are easily damaged under high loads in vigorous exercise. Annually, nearly one out of 1,250 persons worldwide requires surgical reconstruction of their anterior cruciate ligament (ACL)[8,9]. Obtaining grafts that are mechanically strong and integrate sufficiently well with host bone to withstand high loads under vigorous joint motions is both critical and challenging for effective functional recovery of force-transmitting connective tissues[4,10].

Autografts and allografts are considered optimal choices for ACL surgical reconstruction because they are intrinsically bioactive, promoting cell proliferation and new tissue growth. However, they are generally scarce and may suffer from potential risks such as donor-site morbidity and disease transmission[3,6,11]. Synthetic polymeric grafts such as poly(ethylene terephthalate) (PET), polycaprolactone and silk have also been designed for clinical practice[3,12]. However, polymeric grafts have poor longevity because they generally degrade

[1]State Key Laboratory of Molecular Engineering of Polymers, Department of Macromolecular Science and Laboratory of Advanced Materials, Fudan University, Shanghai, China. [2]Department of Orthopedic Sports Medicine, Huashan Hospital, The Sports Medicine Institute, Fudan University, Shanghai, China. [3]State Key Laboratory of Genetic Engineering and Collaborative Innovation Center for Genetics and Development, School of Life Sciences, Institute of Biomedical Sciences, Human Phenome Institute, Zhongshan Hospital, Fudan University, Shanghai, China. [4]Department of Integrative Medicine, Huashan Hospital, The Academy of Integrative Medicine, Fudan University, Shanghai, China. [5]Department of Aeronautics and Astronautics, Fudan University, Shanghai, China. [6]Vision Research Laboratory, School of Life Sciences, State Key Laboratory of Medical Neurobiology, Collaborative Innovation Centre for Brain Science, Fudan University, Shanghai, China. [7]These authors contributed equally: Liyuan Wang, Fang Wan, Yifan Xu, Songlin Xie, Tiancheng Zhao, Fan Zhang. ✉e-mail: cshiyi11@gmail.com; sunxm@fudan.edu.cn; peiningc@fudan.edu.cn; chend@fudan.edu.cn; penghs@fudan.edu.cn

https://doi.org/10.1038/s41565-023-01394-3

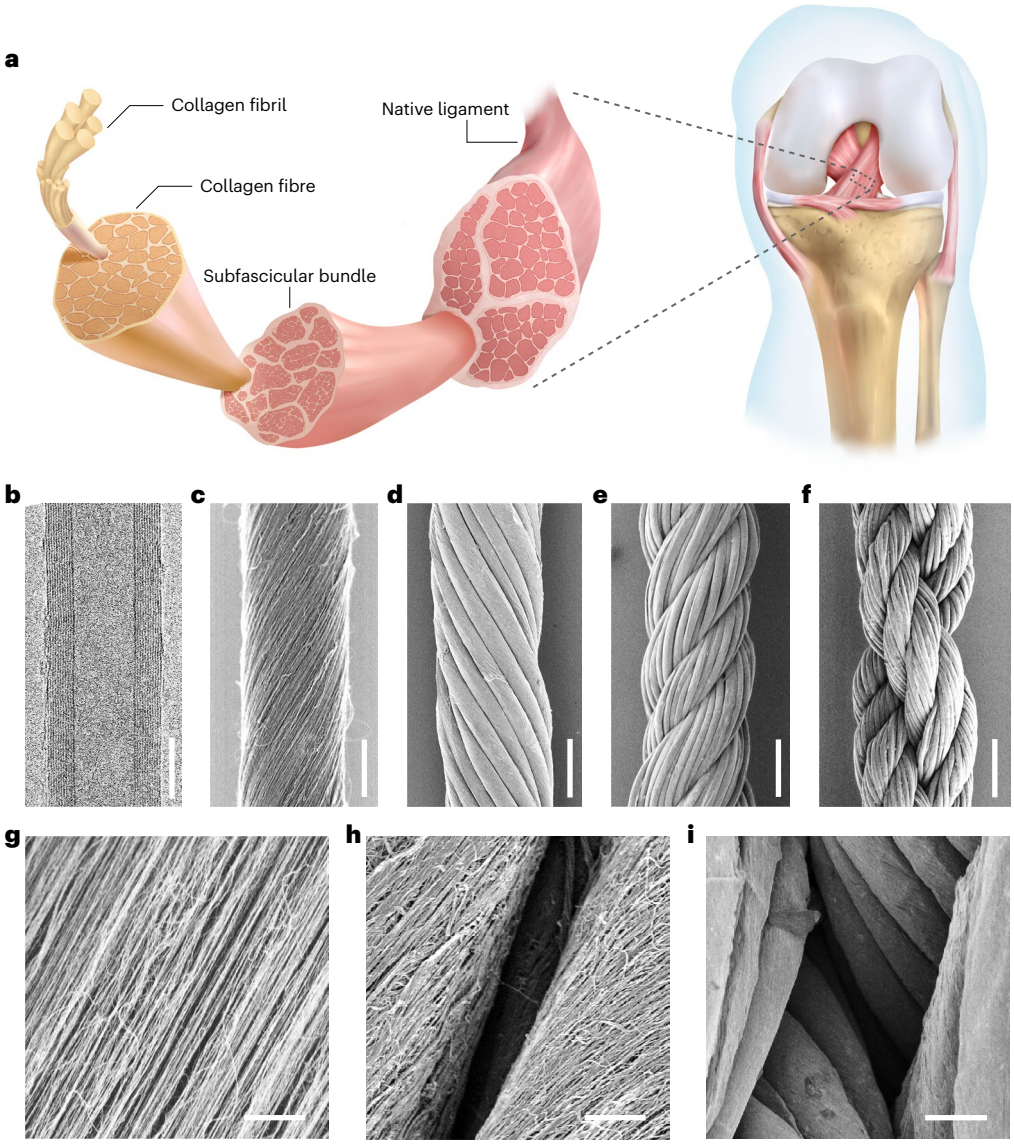

Fig. 1 | Hierarchical structure of native ligament and an HHF. a, Schematic illustration of native ACL connecting the femur and tibia. Native ligament is hierarchically composed of subfascicular bundles made up of collagen fibres, which are organized bundles of collagen fibrils. **b**, TEM image of a multiwalled CNT (diameter, ~10 nm). Scale bar, 5 nm. **c**, SEM image of a primary fibre formed from continuously twisting an aligned CNT sheet. Scale bar, 10 µm. **d**, SEM image of a secondary fibre (diameter, ~80 µm) obtained by twisting together 30 primary fibres, which end up helically aligned around the axial direction. Scale bar, 40 µm. **e**, SEM image of an HHF (diameter, ~160 µm) twisted from four secondary fibres. Scale bar, 80 µm. **f**, SEM image of an HHF being folded and twisted into a larger fibre with a double-helix structure. Scale bar, 150 µm. **g**, Magnified view of **c** showing how the aligned CNTs form nanometre-scale channels. Scale bar, 1 µm. **h**, Magnified view of **d** showing how neighbouring primary fibres form micrometre-scale channels. Scale bar, 1 µm. **i**, Magnified view of **f** showing how micrometre-scale channels form among secondary fibres. Scale bar, 10 µm.

and/or weaken in vivo[13,14]. More importantly, synthetic polymers are inert and poor at inducing osteogenesis for graft-to-bone healing, leading to bone tunnel enlargement and graft failure that require revision surgeries[15,16]. Biofunctionalization of inert polymer grafts by seeding them with cultured cells and/or transforming growth factor is widely used to enhance osteogenesis[12,17,18]. However, inadequate osseointegration remains a common experience. These procedures are also expensive and can cause unexpected complications such as ectopic bone formation and inflammation[12,14]. Realizing strong and lasting high-performance grafts that integrate effectively with hard bones remains an unmet need.

The unique and high-performing functions of natural tissues are attributed to their anisotropic structure, which is typically composed of hierarchically organized organic components[19,20]. The ligament, for instance, is a hierarchy of nanometre-sized collagen fibrils organized into micrometre-sized collagen fibres and subfascicular bundles[7] (Fig. 1a). The longitudinally aligned arrangement of collagen fibrils and fibres strengthens the ligament, allowing it to transfer high stress loads from joint motions. Nanometre-scale channels between collagen fibrils and micrometre-scale channels between collagen fibres and bundles form a favourable environment for cell attachment and proliferation, and promote the recruitment differentiation of mesenchymal stem cells (MSCs)[21–24]. We hypothesized that if this hierarchically aligned structure could be assembled from strong one-dimensional building blocks to form multiscale channels, it would be possible to obtain strong synthetic grafts that also offer the right environment for cell and tissue growth to achieve effective biointegration.

In this study, we report such a high-performing artificial ligament comprising carbon nanotubes (CNTs) assembled into hierarchical

https://doi.org/10.1038/s41565-023-01394-3

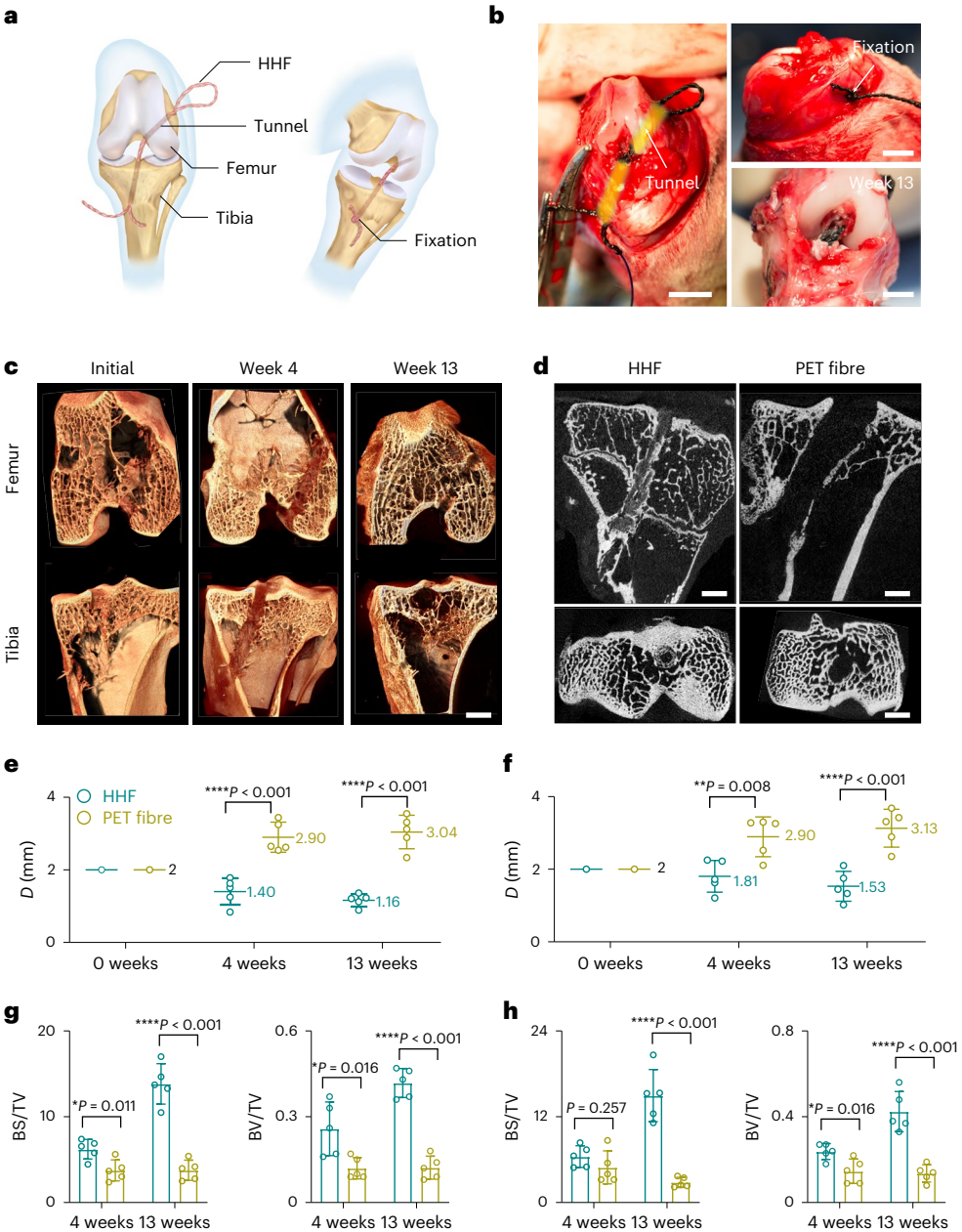

Fig. 2 | ACL reconstruction using an HHF in a rabbit model. a,**b**, Schematic (**a**) and photographs (**b**) showing the procedure of ACL reconstruction surgery using an HHF as an artificial ligament. The HHF is threaded through drilled tunnels (2 mm diameter) and fixed with a knot at the ends. Scale bars in **b**, 1 mm. **c**, Representative three-dimensional μCT reconstructed images of femoral and tibial tunnel 4 and 13 weeks after HHF implantation show new bone tissues are formed. Images are representative of eight independent experiments. Scale bar, 2 mm. **d**, Typical μCT images of femoral tunnel scanned in a coronal plane (top row) and tibial tunnel scanned in an axial plane (bottom row) after implanting an HHF (left) or a clinical PET fibre (right) for 13 weeks. Tunnel defects are recovered in the HHF group, while tunnel enlargement occurs in the PET fibre group. Images are representative of eight independent experiments. Scale bar, 2 mm. **e**,**f**, Average diameters of tibial (**e**) and femoral (**f**) tunnels after implanting an HHF (green symbols) or a clinical PET fibre (yellow symbols) graft for 4 and 13 weeks. Continuous narrowing and enlargement of bone tunnels are quantitatively indicated for the HHF and graft groups, respectively. $n = 5$ biologically independent experiments for each group. **g**,**h**, Ratios of bone volume (BV) to total volume (TV) and bone surface (BS) to TV in tibial (**g**) and femoral (**h**) tunnels after implantation for 4 and 13 weeks. $n = 5$ biologically independent experiments for each group. Statistical significance in **e**–**h** was determined by unpaired two-tailed *t*-test: n.s., not significant ($P > 0.05$), $^{*}P < 0.05$, $^{**}P < 0.01$, $^{***}P < 0.005$ and $^{****}P < 0.001$. All data are expressed as mean ± s.d.

helical fibres (HHFs) with anisotropic structures resembling native ligament. We show that these HHFs successfully repaired the ACLs in rabbits and sheep, effectively restoring the animals' ability to stand, walk and hop. The nanometre and micrometre channels formed between the aligned fibres were shown to encourage bone regeneration and complete repair of the bone tunnel defects.

Assembly and characterization of HHFs

Like collagen fibrils in native ligament, CNTs form the building blocks of our artificial ligament as they are biocompatible, lightweight and have high tensile strength and a large surface area[25–28]. The CNTs, which have a multiwalled structure and a diameter of ~10 nm (Fig. 1b), were prepared by chemical vapour deposition and floating chemical

https://doi.org/10.1038/s41565-023-01394-3

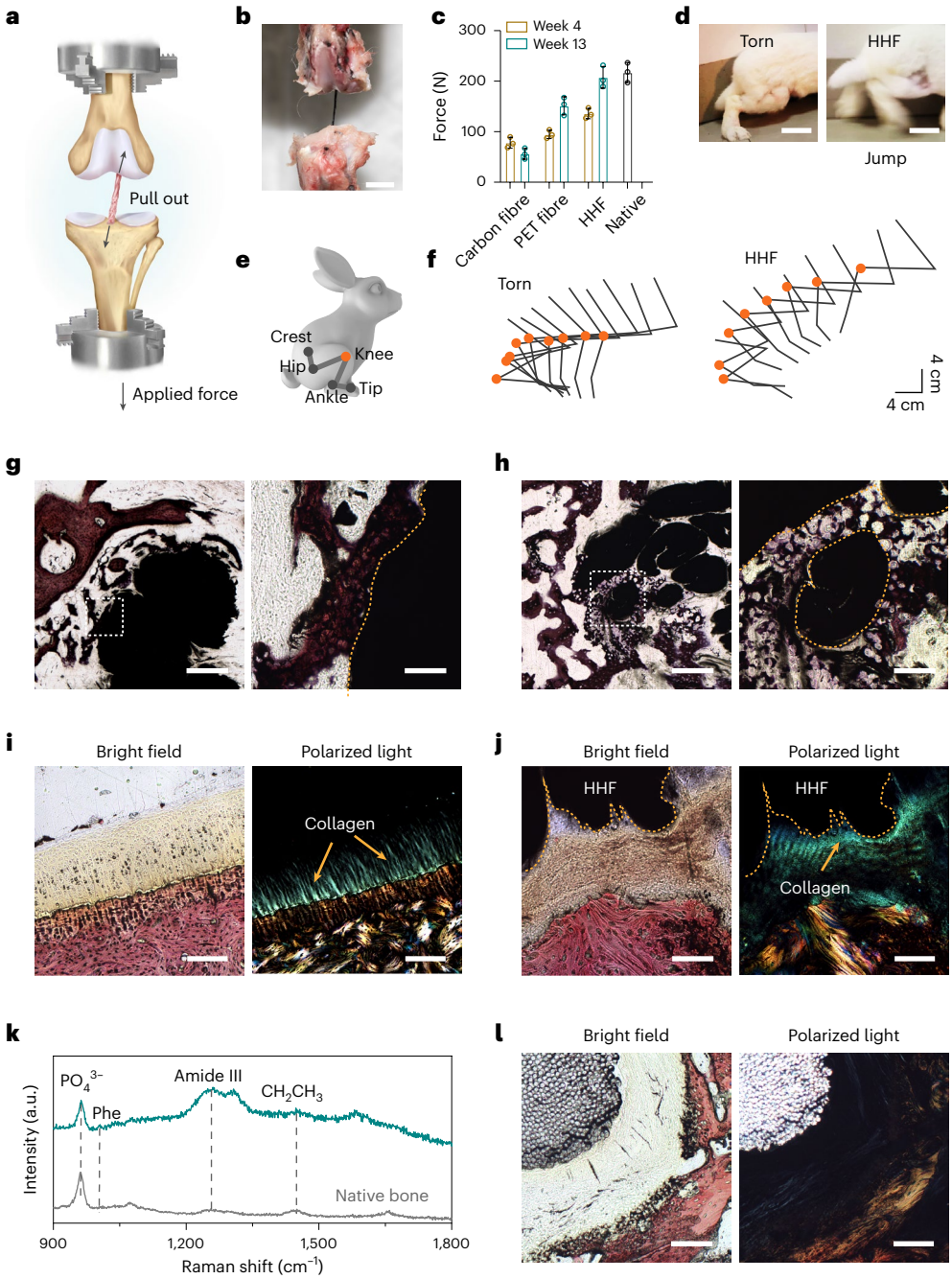

Fig. 3 | Biointegration of HHF grafts and controls. a,**b**, Schematic (**a**) and photograph (**b**) of pulling-out test for the implanted grafts. Pull-out force is traced as the grafts are pulled out from the bone tunnel. Scale bar, 1 cm. **c**, The maximum pull-out force of native ligament, HHF, carbon fibre and PET fibre grafts with the same diameter after implantation for 4 and 13 weeks. $n = 3$ biologically independent experiments for each group. All data are expressed as mean ± s.d. **d**, Photographs comparing the hindlimb before (left) and 13 weeks after (right) ACL reconstruction using an HHF as an artificial ligament. **e**, Schematic of the right hindlimb of a rabbit and the key joints relevant for movement. The knee is marked with an orange dot for kinematic analysis. **f**, Schematics comparing the hindlimb kinematics during movement for a torn and reconstructed ligament. Consistent with images in **e**, rabbits with HHFs as artificial ligaments completed the jump ($n = 20$). **g**,**h**, H&E-stained images of bone tunnels after HHF implantation for 4 weeks (**g**) and 13 weeks (**h**). Newly formed bones fill the tunnels between the defected bone and HHF after 4 weeks (**g**), and new bone grows into the channels among primary fibres of the HHF after 13 weeks. Right panels: magnified images of dashed boxes in left panels. Scale bars, 500 µm (left); 100 µm (right). **i**,**j**, Picrosirius-red-stained slices of native bone tissues (**i**) and bone tunnel implanted with an HHF (**j**) under bright-field and polarized light. Anisotropically arranged collagen components (green in right panel of **j**) resembling those (green in right panel of **i**) in native bone are observed at the interfacial region between the HHF and host bone. Scale bar, 100 µm. **k**, Raman analysis of native bone (grey) and the interface between newly formed bone and implanted HHF graft (green) after 13 weeks showing the characteristic PO_4^{3-} peaks for calcium phosphate and amide III for collagen. **l**, Picrosirius-red-stained slices of bone tunnel implanted with a PET graft show almost no collagen at the PET fibre and host bone interface. Scale bar, 100 µm.

vapour deposition methods, and were assembled into micron-sized helical primary CNT fibres (Fig. 1c) that resemble collagen fibres by continuously twisting aligned CNT sheets[29,30] (Supplementary Fig. 1). When these multi-ply primary fibres are twisted together, we obtained submillimetre-scale secondary CNT fibres that are equivalent to subfascicular bundles in native ligament (Fig. 1d). Further twisting together

secondary fibres resulted in our millimetre-scale HHF graft (Fig. 1e,f). The number of yarn wet snarls was used to evaluate the residual force[31]. The yarn wet snarls of the HHFs were almost 0 turn/25 cm and this was stably maintained for over 1 week, indicating that negligible residual stress was produced after formation of the stable double-helix structure. The diameter of the HHFs can be readily tuned by changing the numbers of primary and secondary fibres; channels of resultant fibres ranging from tens to hundreds of nanometres formed among the aligned CNTs (Fig. 1g). Similarly, micrometre-scale channels are found among the aligned primary fibres (Fig. 1h) and secondary fibres (Fig. 1i) of the hierarchically assembled helix.

The CNT fibres used to construct the HHFs have mechanical properties superior to those of clinical polyester fibres and autogenous ligaments[13,14,32] (Supplementary Note 2), and are also structurally stable, withstanding 1,000,000 cycles of continuous bending and complex deformations (Extended Data Fig. 1). HHFs exhibit similar moduli (0.472 ± 0.12 GPa) and stiffness (79.43 ± 7.46 N mm^{-1}) to native ligaments[33,34] (Supplementary Note 3). Consistent with this, finite-element simulation of stress distribution in the HHFs suggested that hierarchical channels inside can effectively accommodate deformations of the constituent CNTs[28] (Supplementary Note 4). This mechanical profile makes the HHFs intrinsically durable and suitable for load-bearing grafts. Moreover, for in vivo use, systematic experimental analyses demonstrated that HHFs were biocompatible and safe at both the molecular and histological levels over the long term (Supplementary Note 5).

HHFs encourage osseointegration in vivo

To evaluate the biointegration of HHFs with native bones, we implanted HHFs in a classic rabbit ACL reconstruction model. Following a standard surgical procedure[35] (see Methods for details), tunnels (2 mm in diameter) were drilled in the femur and tibia (Supplementary Figs. 6 and 7) and HHFs (diameter, 1.5 mm) were threaded through the tunnels (Fig. 2a,b). Carbon fibres were chosen as a control group to verify that the nanostructure of HHFs can promote osseointegration (Supplementary Fig. 8). To counteract the complex biological effects, we chose helical PET fibres (the current state-of-the-art synthetic ligament grafts) as control groups to compare bone-repairing performances with the HHFs. All the grafts were implanted into the tunnels under the same conditions.

Microcomputed tomography (μCT) imaging shows that both femoral and tibial tunnels narrowed significantly after HHF implantation (Fig. 2c,d). The tibial tunnels narrowed by 29.9% after 4 weeks and by 41.9% after 13 weeks (Fig. 2e and Extended Data Fig. 4a). At week 13, the average diameter (1.16 mm) of the tibial tunnel was less than the diameter of the HHFs (1.5 mm); newly formed bones had completely occupied the tunnel space and some had also grown into the HHFs. The regenerated bone had the same tubular microstructure as native bone and no clear boundaries were seen between the HHFs and the new bone, indicating that strong osseointegration had occurred[36] (Fig. 2d). An obvious narrowing was also observed in the femoral tunnel (Fig. 2f).

In contrast, obvious enlargements both in femoral and tibial tunnels occurred after implantation of PET fibres. The tibial tunnels enlarged by 45.0% after 4 weeks and by 52.1% after 13 weeks of implantation (Fig. 2e). Such a continued enlargement resulting from the lack of osteogenesis will eventually cause implant failure[6,15]. Commercially available carbon fibre grafts also displayed a similar bone tunnel enlargement (Extended Data Fig. 4b). More seriously, the implanted carbon fibre ruptured at week 13 due to poor flexibility (Extended Data Fig. 4d). Quantitative analysis indicated that both the ratios of bone volume to total volume (BV/TV) and bone surface to total volume (BS/TV) for the HHF group increased with postoperative time (Fig. 2g,h). The BV/TV and BS/TV values for HHF were approximately three times higher than for the PET fibre and carbon fibre groups (Fig. 2g,h and Extended Data Fig. 4c). The average BV/TV ratio (0.42) of the regenerated bone at week 13 for HHFs was similar to the values of native tibia and femur in a rabbit model[37]. The above comparisons of bone repair between the HHF and control groups suggested that the nanometre channels played an important role in osseointegration, which is further verified by the additional groups of hierarchical helical PET fibres with both nanometre and micrometre channels and helical PET fibres with only micrometre channels (Supplementary Note 9).

To quantify the interfacial strength between HHFs and adjacent native bone, we measured the pull-out force, that is, the binding force required to pull out the HHF implant from the bone tunnel, to show the osseointegration degree[38–40] (Fig. 3a,b). In week 4, the implanted HHFs showed a pull-out force three times higher (~150 N) than those between allografts and bones[41,42] (Supplementary Fig. 9). After the HHFs had been implanted for longer times, these grafts required more force to pull out as shown by the high failure force of ~200 N in week 13, 3.6 times higher than that between carbon fibres and bone, and 1.4 times higher than that between PET fibres and bone (Fig. 3c and Extended Data Fig. 5a). These values are similar to the forces required to break a typical native ligament, indicating good bone–graft integration. Scanning electron microscopy (SEM) images further showed abundant regenerated tissues on the pulled-out HHF graft, whereas a smooth surface without attached tissues was seen on the pulled-out PET fibres (Extended Data Fig. 5b),

Fig. 4 | HHF promotes osteogenesis. a, GO and KEGG enrichment based on proteomics analysis of MSCs cultured on HHFs and helical PET fibres show upregulated osteogenesis-related signalling pathways for the four time points (hour 6, day 1, day 3 and day 5). $n = 5$ biologically independent experiments for each group. **b**, Heatmap analysis of differentially expressed proteins related to osteogenesis of MSCs cultured on HHFs and helical PET fibres for the above four time points. $n = 5$ biologically independent experiments for each group. **c**,**d**, On day 5, MSCs cultured on HHFs expressed higher amounts of typical osteogenesis-related proteins (**c**) and genes (**d**) than those cultured on helical PET fibres. Horizontal dotted lines in **c** and **d** represent mean of helical PET fibre group. $n = 5$ biologically independent experiments for each group. Data in **c** and **d** are expressed as mean ± s.d. Statistical significance in **c** and **d**) was determined by unpaired two-tailed *t*-test: n.s., not significant ($P > 0.05$), *$P < 0.05$, **$P < 0.01$, ***$P < 0.005$ and ****$P < 0.001$. **e**, GO and KEGG enrichment based on proteomic analysis of MSCs show upregulated osteogenesis-related signalling pathways for different pairwise comparisons (carbon component: helical carbon fibre versus helical PET fibre; micrometre channel: helical PET fibre versus PET plate; nanometre channel: HHF versus helical carbon fibre). $n = 5$ biologically independent experiments for each group. **f**, Heatmap analysis of differentially expressed proteins related to osteogenesis of MSCs cultured on PET plate, helical PET fibre, helical carbon fibre and HHF. $n = 5$ biologically independent experiments for each group. **g**,**h**, MSCs cultured on PET plate, helical PET fibre, helical carbon fibre and HHF for 5 days express different levels of typical osteogenesis-related proteins in the MAPK (**g**) and WNT signalling pathways (**h**). Protein expression is increased in HHF and associated with other subgroups (PET plate, helical PET fibre and helical carbon fibre). Horizontal dotted lines in **g** and **h** represent mean of PET plate group. $n = 5$ biologically independent experiments for each group. Data in **g** and **h** are expressed as mean ± s.d. Statistical significance in **g** and **h** was determined by unpaired two-tailed *t*-test between two groups and one-way ANOVA among multiple groups: n.s., not significant ($P > 0.05$), *$P < 0.05$, **$P < 0.01$, ***$P < 0.005$ and ****$P < 0.001$. **i**, Schematic illustrating how HHF promotes osteogenesis via the MAPK, WNT and TGF-β signalling pathways. **j**, Heatmap analysis of differentially expressed proteins obtained from rabbit joints implanted with HHFs and helical PET fibres for 2 weeks. $n = 3$ biologically independent experiments for each group. Pathway enrichment analysis in **a** and **e** was performed by DAVID (https://david.ncifcrf.gov/) and ConsensusPathDB (http://cpdb.molgen.mpg.de/CPDB). *P* value is calculated based on the hypergeometric distribution and the significant pathway ($P < 0.05$) was used for further study.

https://doi.org/10.1038/s41565-023-01394-3

consistent with cell culture results showing far less osteoblast adhesion and proliferation on PET than on CNT sheets (Extended Data Fig. 5c). Due to the strong interfacial strength caused by bone regeneration on HHFs, all eight rabbits implanted with HHFs as artificial ligaments recovered and were able to complete free jumps 13 weeks after ACL reconstruction surgery (Fig. 3d–f, Extended Data Fig. 5d and Supplementary Movie 1). In contrast, control rabbits with torn ligaments on their hindlimbs failed to complete a jump (Supplementary Movie 2).

Furthermore, consistent with μCT and biomechanical findings, haematoxylin and eosin (H&E)-stained sections revealed that regenerated bone had grown into the implanted HHFs. After 4 weeks of implantation, newly formed bones were observed at the interfacial region between HHFs and native bone (Fig. 3g) and the bone density around HHFs increased after 13 weeks (Fig. 3h). Most of the newly formed bone grew into the micrometre-scale channels between the primary fibres, which helped anchor the HHF grafts to the host bone.

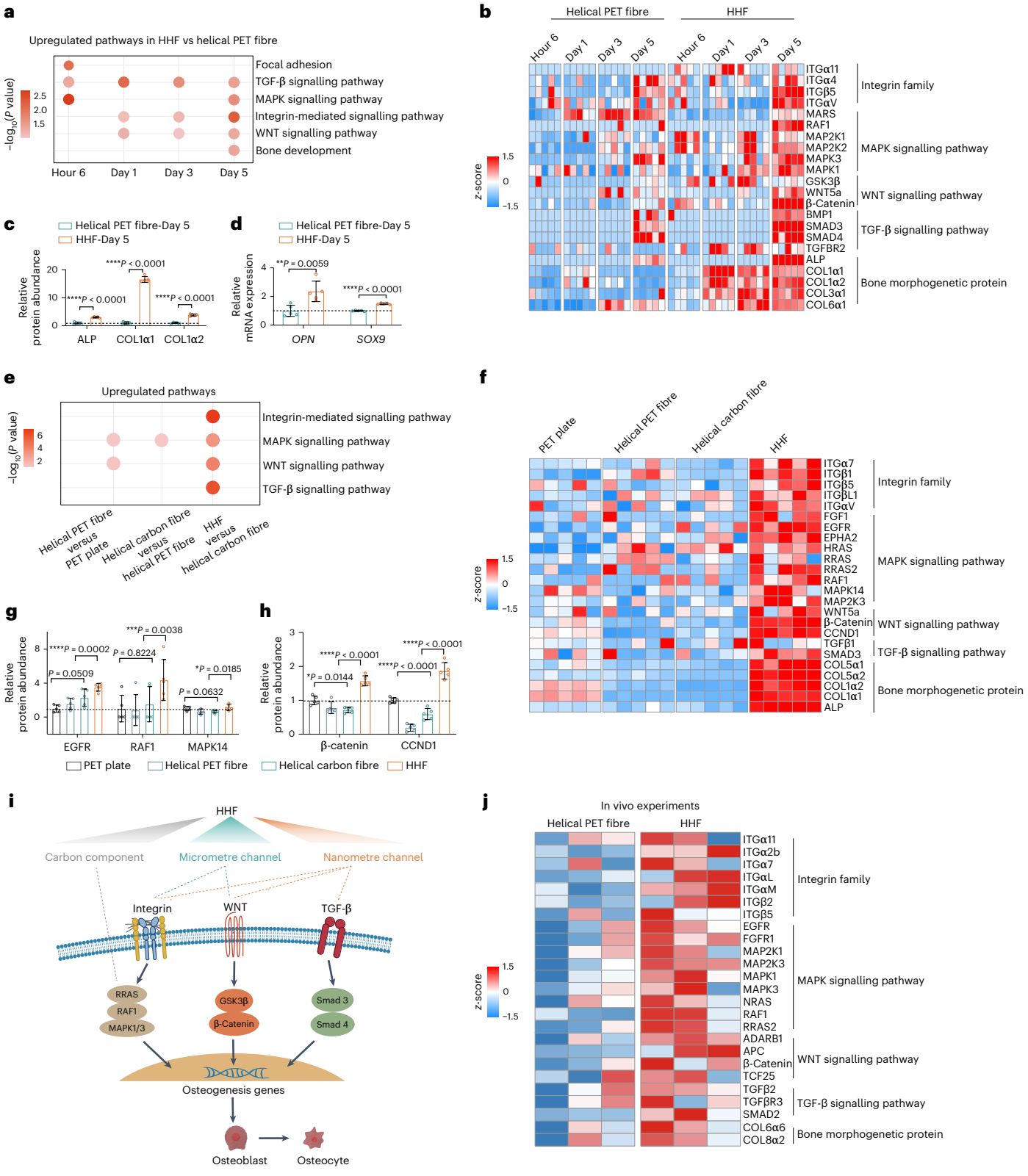

https://doi.org/10.1038/s41565-023-01394-3

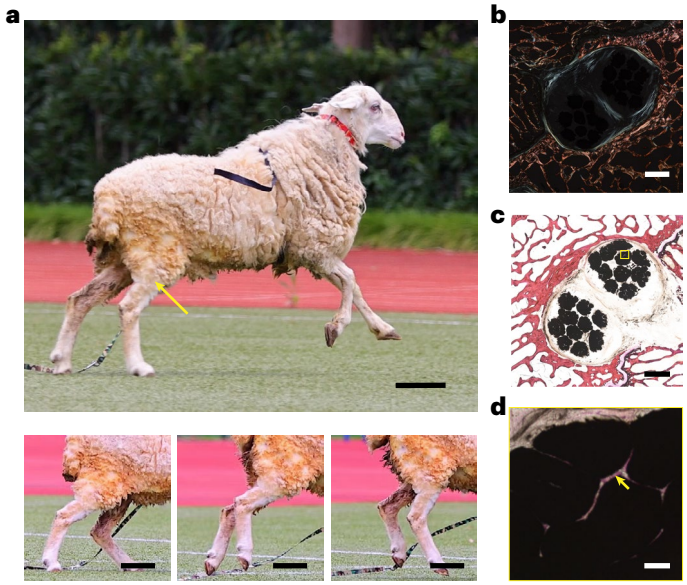

Fig. 5 | ACL reconstruction using HHF graft restores mobility in a large animal (sheep) model. a, Photographs of a postoperative sheep running with a normal posture in month 9. Yellow arrow indicates the ligament on the right leg reconstructed with an HHF graft. Scale bars, 10 cm. **b**, Picrosirius-Red-stained slice of the bone tunnel at month 9 shows collagen tissue in the interfacial region between the HHF and native bone. Scale bar, 3 mm. **c**, H&E-stained image of the bone tunnel in month 9 shows dense, newly formed bone tissues regenerated in the interfacial region between the HHF and native bone. Scale bar, 3 mm. **d**, Magnified view of yellow box in **c** shows newly formed bone tissues (yellow arrow) in the channels within the HHF. Scale bar, 100 μm.

In particular, a thick layer of anisotropic collagen resembling those in native bone tissues was observed at the interfacial region between HHFs and host bone (Fig. 3i,j). Collagen formation is fundamental for the calcification and mineralization of bones[43]. Raman spectra further verified the formation of hydroxyapatite and collagen tissue at the interfacial region: characteristic signals of PO_4^{3-} for calcium phosphate and amide III for collagen were both detected[44,45] (Fig. 3k). In contrast, little to no regenerated bone and collagen was seen at the interfacial region of PET fibre and carbon fibre grafts (Fig. 3l and Extended Data Fig. 5e,f).

We further performed a series of histological analyses to understand the osseointegration process induced by the implanted HHFs. The histological results showed HHFs could promote the activities of both osteoblasts and osteoclasts to enhance bone modelling and remodelling, and collagen bundles could be gradually formed around and inside the HHFs at the early stage of osseointegration (Extended Data Fig. 6a–c). Moreover, the CD31/vascular endothelial growth factor (VEGF)[46,47] and calcitonin gene-related peptide (CGRP)[48]-stained images indicated the formation of vessels and nerves in week 4 (Extended Data Fig. 6d,e).

Compared with the enlargement of bone tunnel defects observed with PET grafts, the tunnel defect was continuously repaired to 0.86 mm after a longer time (18 months) of HHF implantation, and dense bone tissue completely occupied the tunnel and even the micrometre channels of the HHFs (Extended Data Fig. 7). Moreover, both vessels and nerves were formed in the micrometre channels of the HHFs (Supplementary Figs. 16 and 17), whereas few vessels and nerves occurred in the PET grafts.

HHFs induce expression of osteogenic proteins

To understand how HHFs induce osteogenesis, we cultured MSCs on HHF and PET fibres for different periods of time and simultaneously performed both proteomic and transcriptomic analysis to screen for all possible osteogenesis-related proteins and genes that might be induced by HHFs (see Methods for details).

As shown in Fig. 4a,b, integrins that mediate focal adhesions and mitogen-activated protein kinases (MAPKs, including MAP2K1 and MAP2K2) began to upregulate at hour 6 in the HHF group. Osteogenesis-related protein COL1α1/COL1α2 and proteins relevant to the wingless-integrated (WNT) signalling pathway appeared on days 1 and 3 (Fig. 4b). In particular, WNT, transforming growth factor-β (TGF-β) and integrin-mediated signalling pathways were highly enriched (Fig. 4a). On day 5, osteogenesis-related proteins, genes and osteoblast markers were significantly upregulated in the HHF group. For instance, alkaline phosphatase (ALP, an early marker for osteogenic differentiation) and COL1 (which stimulates osteoblast differentiation), at the protein level, and secreted phosphoprotein 1 (*OPN*, a matrix protein produced before mineralization) and sex-determining region Y-box 9 (*SOX9*, a transcription factor to control skeletal development), at the mRNA level, were highly overrepresented in the HHF group (Fig. 4c,d). Both proteomic and transcriptomic results (Extended Data Fig. 8a,b) indicate that HHFs promoted osteogenesis via MAPK, WNT and TGF-β signalling pathways. Because cells are inherently sensitive to their microenvironment, these signalling pathways were probably activated in response to the topography (that is, the hierarchically arranged nanometre and micrometre channels) and chemistry (that is, the carbon content) of the HHFs.

To investigate how the topographical and chemical features of HHFs differentially activate the signalling pathways, we pairwise compared the osteogenic differentiation of MSCs on six control substrates with designed components and topographical features (Extended Data Fig. 8c). The controls included: (1) carbon plates with carbon components but without micrometre and nanometre channels, (2) helical carbon fibres with carbon components and only micrometre channels, (3) HHFs with carbon components and both micrometre and nanometre channels, (4) PET plates without micrometre and nanometre channels, (5) helical PET fibres with only micrometre channels and (6) hierarchical helical PET fibres based on PET and with micrometre and nanometre channels. First, both the comparative proteomics and transcriptomics of helical carbon fibres versus helical PET fibres (Fig. 4e and Extended Data Fig. 8f), and proteomics in HHFs versus hierarchical helical PET fibres (Supplementary Fig. 20) indicated the carbon components could activate the MAPK signalling pathway. Second, comparison in both helical PET fibres versus PET plates and helical carbon fibres versus carbon plates revealed that the WNT signalling pathway could be induced by micrometre channels (Fig. 4e and Supplementary Fig. 18). Third, comparing HHFs and helical carbon fibres showed that nanometre channels dramatically upregulated all the major osteogenic pathways, including the integrin, MAPK, WNT and TGF-β signalling pathways (Fig. 4e). Typical osteogenesis-related proteins including EGFR, RAF1 and MAPK14 in the MAPK signalling pathway, β-catenin and CCND1 in the WNT signalling pathway, and TGF-β1 and SMAD3 in the TGF-β signalling pathway were overrepresented in the HHF group (Fig. 4f–h). Similar results were seen at the mRNA level (Extended Data Fig. 8d,e). Comparisons between hierarchical helical PET fibres and helical PET fibres further verified that the nanometre channels could activate the integrin, WNT and TGF-β signalling pathways (Supplementary Fig. 19). Based on all the above pairwise comparisons, we conclude that HHFs, as a carbon material with both micrometre and nanometre channels, can activate osteogenic-related signalling pathways (Fig. 4i), and that nanometre channels are more osteogenic than micrometre channels and carbon components.

We further implanted HHFs and helical PET fibres into rabbits and performed proteomic analysis in vivo. The results showed that the MAPK, WNT and TGF-β signalling pathways were significantly upregulated in the HHF group (Fig. 4j and Extended Data Fig. 8g), accompanied by the upregulation of typical osteogenesis-related proteins. The proteomic analysis in vivo also indicated upregulated collagen in the HHF group, which is consistent with the Masson–Goldner- and

Picrosirius-Red-stained results. Together, these results demonstrate that HHFs can induce osteogenesis via integrin-linked MAPK, WNT and TGF-β signalling pathways both in vitro and in vivo.

HHFs restore movement in large animals

Assessment of the in vivo integration and mechanical performance of HHFs in large animal models is necessary to advance human clinical trials of this material. We further implanted HHFs in a sheep ACL reconstruction model (Supplementary Figs. 21 and 22). Consistent with the rabbit model, the tibial tunnel narrowed by over 20% after 13 weeks of HHF implantation, while obvious tunnel enlargement (from initial 7.5 mm to 9 mm) occurred for PET fibres at week 13 (Extended Data Fig. 9a,b). More importantly, an enlargement of over 50% was observed at the end of the bone tunnel with PET fibres. For commercial LARS (Ligament Advanced Reinforcement System) grafts (Scientific Research and Application Laboratory) made from PET fibres[49], similar bone tunnel enlargement (~30%) was observed after 3 months of implantation (Supplementary Fig. 23). Further histological examination of Picrosirius-red-stained slice under polarized light showed dense collagen tissue in the interfacial region between the HHFs and native bone at week 13, and newly formed bone tissues were regenerated in the channels within the HHFs (Extended Data Fig. 9d–f), while only fibrous tissues and few new bones were aggregated around and inside LARS grafts and allografts[49–51]. Sheep treated with HHF grafts could stand and walk with a normal gait without limping after 13 weeks (Extended Data Fig. 9c and Supplementary Movie 3). Continuous repair of bone tunnel defects was further verified by evaluating the sheep with longer HHF implantation times of 9 and even 21 months, and observing that the animals were able to run and jump normally (Fig. 5, Supplementary Fig. 24 and Supplementary Movie 4). These results indicate that strong osteogenesis occurred even in a large animal model.

Conclusion

The results presented here demonstrate that hierarchically arranged CNT fibres integrate remarkably well with native bone and are sufficiently strong to serve as artificial ligaments. When used to replace torn ACLs in rabbits, the bone tunnel defects were completely repaired by the regenerated bone, in strong contrast to >50% tunnel enlargement for clinical polymer grafts. In addition, these fibres encouraged the formation of new bone in the femoral and tibial tunnels. The regenerated bone showed similar microstructures to native bone. We show osteogenesis on these fibres is driven by their multiscale channels and carbon component. This work shows great promise for the clinical translation of hierarchically helical artificial ligaments to human beings, opening up a new avenue to solve the urgent clinical problem for repairing the ligament–bone joint to withstand high and dynamic stress loading. We believe this strategy of twisting materials into hierarchical assemblies with multiple length scales may be generalized to other biocompatible and mechanically strong one-dimensional nanomaterials or micromaterials to obtain similar high-performance artificial tissues.

Online content

Any methods, additional references, Nature Portfolio reporting summaries, source data, extended data, supplementary information, acknowledgements, peer review information; details of author contributions and competing interests; and statements of data and code availability are available at https://doi.org/10.1038/s41565-023-01394-3.

References

1. Meyers, M. A., McKittrick, J. & Chen, P. Y. Structural biological materials: critical mechanics–materials connections. *Science* **339**, 773–779 (2013).
2. Rossetti, L. et al. The microstructure and micromechanics of the tendon–bone insertion. *Nat. Mater.* **16**, 664–670 (2017).
3. Rinoldi, C., Kijenska-Gawronska, E., Khademhosseini, A., Tamayol, A. & Swieszkowski, W. Fibrous systems as potential solutions for tendon and ligament repair, healing, and regeneration. *Adv. Healthc. Mater.* **10**, 2001305 (2021).
4. Gracey, E. et al. Tendon and ligament mechanical loading in the pathogenesis of inflammatory arthritis. *Nat. Rev. Rheumatol.* **16**, 193–207 (2020).
5. Musahl, V. & Karlsson, J. Anterior cruciate ligament tear. *N. Engl. J. Med.* **380**, 2341–2348 (2019).
6. No, Y. J., Castilho, M., Ramaswamy, Y. & Zreiqat, H. Role of biomaterials and controlled architecture on tendon/ligament repair and regeneration. *Adv. Mater.* **32**, 1904511 (2020).
7. Parmar, K. Tendon and ligament: basic science, injury and repair. *Orthop. Trauma.* **32**, 241–244 (2018).
8. Baawa-Ameyaw, J. et al. Current concepts in graft selection for anterior cruciate ligament reconstruction. *EFORT Open Rev.* **6**, 808–815 (2021).
9. Tang, Y. et al. Biomimetic biphasic electrospun scaffold for anterior cruciate ligament tissue engineering. *Tissue Eng. Regen. Med.* **18**, 915–915 (2021).
10. Laranjeira, M., Domingues, R. M. A., Costa-Almeida, R., Reis, R. L. & Gomes, M. E. 3D mimicry of native-tissue-fiber architecture guides tendon-derived cells and adipose stem cells into artificial tendon constructs. *Small* **13**, 1700689 (2017).
11. Kawakami, Y. et al. A cell-free biodegradable synthetic artificial ligament for the reconstruction of anterior cruciate ligament (ACL) in a rat model. *Acta Biomater.* **121**, 275–287 (2021).
12. Freedman, B. R. & Mooney, D. J. Biomaterials to mimic and heal connective tissues. *Adv. Mater.* **31**, 1806695 (2019).
13. Wang, Z. et al. Functional regeneration of tendons using scaffolds with physical anisotropy engineered via microarchitectural manipulation. *Sci. Adv.* **4**, eaat4537 (2018).
14. Li, H. G. et al. Functional regeneration of ligament–bone interface using a triphasic silk-based graft. *Biomaterials* **106**, 180–192 (2016).
15. Tulloch, S. J. et al. Primary ACL reconstruction using the LARS device is associated with a high failure rate at minimum of 6-year follow-up. *Knee Surg. Sports Traumatol. Arthrosc.* **27**, 3626–3632 (2019).
16. Mayr, R., Rosenberger, R., Agraharam, D., Smekal, V. & El Attal, R. Revision anterior cruciate ligament reconstruction: an update. *Arch. Orthop. Trauma Surg.* **132**, 1299–1313 (2012).
17. Cross, L. M., Thakur, A., Jalili, N. A., Detamore, M. & Gaharwar, A. K. Nanoengineered biomaterials for repair and regeneration of orthopedic tissue interfaces. *Acta Biomater.* **42**, 2–17 (2016).
18. Ducheyne, P., Mauck, R. L. & Smith, D. H. Biomaterials in the repair of sports injuries. *Nat. Mater.* **11**, 652–654 (2012).
19. Koons, G. L., Diba, M. & Mikos, A. G. Materials design for bone-tissue engineering. *Nat. Rev. Mater.* **5**, 584–603 (2020).
20. Muller, R. Hierarchical microimaging of bone structure and function. *Nat. Rev. Rheumatol.* **5**, 373–381 (2009).
21. Wang, Y. et al. Functional regeneration and repair of tendons using biomimetic scaffolds loaded with recombinant periostin. *Nat. Commun.* **12**, 1293 (2021).
22. Liu, X. L. & Wang, S. T. Three-dimensional nano-biointerface as a new platform for guiding cell fate. *Chem. Soc. Rev.* **43**, 2385–2401 (2014).
23. Li, Y. L., Xiao, Y. & Liu, C. S. The horizon of materiobiology: a perspective on material-guided cell behaviors and tissue engineering. *Chem. Rev.* **117**, 4376–4421 (2017).
24. Younesi, M., Islam, A., Kishore, V., Anderson, J. M. & Akkus, O. Tenogenic induction of human MSCs by anisotropically aligned collagen biotextiles. *Adv. Funct. Mater.* **24**, 5762–5770 (2014).

25. De Volder, M. F. L., Tawfick, S. H., Baughman, R. H. & Hart, A. J. Carbon nanotubes: present and future commercial applications. *Science* **339**, 535–539 (2013).
26. Bai, Y. X. et al. Super-durable ultralong carbon nanotubes. *Science* **369**, 1104–1106 (2020).
27. Zhang, R. F., Zhang, Y. Y. & Wei, F. Horizontally aligned carbon nanotube arrays: growth mechanism, controlled synthesis, characterization, properties and applications. *Chem. Soc. Rev.* **46**, 3661–3715 (2017).
28. Wang, L. Y. et al. Functionalized helical fibre bundles of carbon nanotubes as electrochemical sensors for long-term in vivo monitoring of multiple disease biomarkers. *Nat. Biomed. Eng.* **4**, 159–171 (2020).
29. Deng, J. et al. Preparation of biomimetic hierarchically helical fiber actuators from carbon nanotubes. *Nat. Protoc.* **12**, 1349–1358 (2017).
30. Mu, J. K. et al. Sheath-run artificial muscles. *Science* **365**, 150–155 (2019).
31. Duo, X. et al. A novel concept to produce super soft characteristic ring-yarn with structural variation via against-twisting. *J. Nat. Fibers* **19**, 5524–5536 (2022).
32. Aka, C. & Basal, G. Mechanical and fatigue behaviour of artifcial ligaments (ALs). *J. Mech. Behav. Biomed. Mater.* **126**, 105063 (2022).
33. Brennan, D. A. et al. Mechanical considerations for electrospun nanofibers in tendon and ligament repair. *Adv. Healthc. Mater.* **7**, 1701277 (2018).
34. Grana, W. A. et al. An analysis of autograft fixation after anterior cruciate ligament reconstruction in a rabbit model. *Am. J. Sport. Med.* **22**, 344–351 (1994).
35. Bachy, M. et al. Anterior cruciate ligament surgery in the rabbit. *J. Orthop. Surg. Res.* **8**, 27 (2013).
36. Petite, H. et al. Tissue-engineered bone regeneration. *Nat. Biotech.* **18**, 959–963 (2000).
37. Zhao, F. et al. A more flattened bone tunnel has a positive effect on tendon-bone healing in the early period after ACL reconstruction. *Knee Surg. Sports Traumatol. Arthrosc.* **27**, 3543–3551 (2019).
38. Cooper, J. A. et al. Biomimetic tissue-engineered anterior cruciate ligament replacement. *Proc. Natl Acad. Sci. USA* **104**, 3049–3054 (2007).
39. Mengsteab, P. Y. et al. Mechanically superior matrices promote osteointegration and regeneration of anterior cruciate ligament tissue in rabbits. *Proc. Natl Acad. Sci. USA* **117**, 28655–28666 (2020).
40. Liddell, R. S., Liu, Z. M., Mendes, V. C. & Davies, J. E. Relative contributions of implant hydrophilicity and nanotopography to implant anchorage in bone at early time points. *Clin. Oral. Implants Res.* **31**, 49–63 (2020).
41. Dong, S. et al. Decellularized versus fresh-frozen allografts in anterior cruciate ligament reconstruction. *Am. J. Sport. Med.* **43**, 1924–1934 (2015).
42. Bi, F. et al. Anterior cruciate ligament reconstruction in a rabbit model using silk-collagen scaffold and comparison with autograft. *PLoS ONE* **10**, e0125900 (2015).
43. Wang, Y. et al. The predominant role of collagen in the nucleation, growth, structure and orientation of bone apatite. *Nat. Mater.* **11**, 724–733 (2012).
44. Falgayrac, G. et al. Bone matrix quality in paired iliac bone biopsies from postmenopausal women treated for 12 months with strontium ranelate or alendronate. *Bone* **153**, 116107 (2021).
45. Mandair, G. S. & Morris, M. D. Contributions of Raman spectroscopy to the understanding of bone strength. *Bonekey Rep.* **4**, 620 (2015).
46. Yz, A. et al. Spatiotemporal blood vessel specification at the osteogenesis and angiogenesis interface of biomimetic nanofiber-enabled bone tissue engineering. *Biomaterials* **276**, 121041 (2021).
47. Hu, K. & Olsen, B. R. Vascular endothelial growth factor control mechanisms in skeletal growth and repair. *Dev. Dynam.* **246**, 227–234 (2017).
48. Ma, L. et al. CGRP-α application: a potential treatment to improve osseoperception of endosseous dental implants. *Med. Hypotheses* **81**, 297–299 (2013).
49. Parchi, P. D. et al. Anterior cruciate ligament reconstruction with LARS artificial ligament—clinical results after a long-term follow-up. *Joints* **6**, 75–79 (2018).
50. Li, H. et al. Differences in artificial ligament graft osseointegration of the anterior cruciate ligament in a sheep model: a comparison between interference screw and cortical suspensory fixation. *Ann. Transl. Med.* **17**, 1370 (2021).
51. Schmidt, T. et al. Does sterilization with fractionated electron beam irradiation prevent ACL tendon allograft from tissue damage? *Knee Surg. Sports Traumatol. Arthrosc.* **25**, 584–594 (2017).

Methods

Materials preparation

The preparation methods for the CNT fibres are introduced in the Supplementary Information. HHFs were prepared by twisting multi-ply CNT fibres with two ends stabilized, followed by a retwisting process after the two ends were folded together. In addition, PET fibres (Kinetic Medical) and carbon fibres (Toray Industries) were also assembled into the same helical structure as the HHFs by the twisting method. Electrospinning PET films with nanostructure (Foshan Lepton Precision Measurement and Control Technology) were cut into strips with a width of 500 μm and then twisted into helical structures similar to those of the HHFs.

ACL reconstruction on New Zealand white rabbits

Animal experiments were approved by the Institutional Animal Care and Use Committee at Fudan University (number 2019Huashan HospitalJS-118). All animals were housed at the animal care laboratory at the College of Pharmacy in accordance with the regulations set by the National Institutes of Health.

After 2 weeks in quarantine, a total of 85 skeletally mature male New Zealand rabbits (3–3.5 kg at the time of surgery) were included in the study. The animals were randomly divided into three groups: a PET fibre group ($n = 16$), a carbon fibre group ($n = 16$) and an HHF group ($n = 16$). In these groups, the PET and carbon fibre grafts had the same helical structure, diameter (1.5 mm) and length (5.0 cm) as the HHF grafts. The diameter and length were measured by microscopy and with a ruler, respectively. Each group was implanted by different types of grafts described above.

ACL reconstruction surgery was performed on the right knees. Briefly, after the rabbits had been anaesthetized by intravenous administration of 3% pentobarbital (30 mg per kg (body weight)), they were fixed on the operation table in the supine position. A medial 3 cm parapatellar incision was made after skin preparation and disinfection with 2.5% iodophor solution. The skin and subcutaneous tissue was dissected layer by layer. The medial patellar retinaculum was incised and the patellar was dislocated manually to better identify the structure of the right knee joint. The native ACL was exposed and transected at the midsubstance by a sharp scalpel as illustrated in Supplementary Fig. 6a,b. The Lachman test was performed after the procedure with positive results, confirming the discontinuity of the native ACL. The bone tunnels with a diameter of 2.0 mm were created by using a Kirschner wire (2 mm in diameter) to drill from inside out at the site of femoral insertion and then behind the tibial insertion of the ACL (Supplementary Fig. 6c,d). The artificial ligament was pulled into the tunnel with PDS II guide wire (Ethicon). The femoral end of the graft was knotted, and the knot was sutured to the periosteum using No. 4-0 Ethibond (Ethicon). The tibial end of the graft was knotted, and the knot was sutured with the knee in the posterior Lachman test position using No. 4-0 Ethibond. After graft implantation, irrigation and consecutive cycling loads (20 times) were performed, and layered closure with interrupted sutures was used to close the knee capsule, subcutaneous tissue and the skin. All the rabbits were left free to ambulate in their cages after surgery. Intramuscular prophylactic antibiotic injections (800,000 IU of penicillin) and wound cleaning were performed immediately after the operation once a day for 3 days in series.

Biomechanical pull-out tests

The rabbits were divided into five groups: two groups were implanted with HHF grafts for 4 and 13 weeks, two groups were implanted with PET grafts for 4 and 13 weeks, and one control group had no implanted grafts. Each group comprised three rabbits. In these groups, PET fibre and carbon fibre grafts showed the same helical structure, diameter (1.5 mm) and length (5.0 cm) as the HHF grafts. The diameter of all the bone tunnels was the same (2.0 mm). The femur–graft–tibia complexes were removed from the three rabbits in each group for mechanical testing. The soft tissues around the knee joint were carefully removed from the complex to make sure the only connectivity between femur and tibia was the graft. All mechanical tests were conducted with an electronic universal material testing system (AGS-X, Shimadzu). The femur and tibia were secured into the testing apparatus with fixation bolts and dental cement. The ultimate failure load was tested with an elongation rate of 2 mm min^{-1} after 5 N static preloading for 5 min. The test continued until the graft was pulled out of the tunnel. The ultimate failure load was recorded.

μCT evaluation and analysis

After the macroscopic evaluation, specimens of femur–graft–tibia complex were used for μCT (Bruker SkyScan 1176, operated at 65 kV and 380 μA) evaluation with a slicing thickness of 17 μm. The obtained data were used for the image reconstruction of the femur–graft–tibia complexes in the axial direction, which were further imported into CTAn and CTVox. The images were analysed and processed into three-dimensional models via CTVox to analyse the longitudinal section of the femoral and tibial tunnels. Through the CTAn analysis, the average diameter of the tunnel and the variation ratio were calculated. In addition, the BV/TV and BS/TV were analysed.

Histological examination

After μCT scanning, specimens of femur–graft–tibia complex were fixed in 10% formalin for 1 week. Then they were dehydrated with acetone. Every experiment was technically repeated five times. For hard-tissue slicing, the specimens were further dehydrated with an EXAKT 510 dehydration system (EXAKT Technologies). After hydration, the specimens were further embedded in resin by using an EXAKT 520 resin infiltration system. The resin was sectioned with an EXAKT 300 CP cutting system perpendicular to the longitudinal axis of the femur and tibia tunnel, and ground into 10 μm slices with an EXAKT 400 CS grinding system. The sections were stained with H&E and toluidine blue to observe the growth of bony trabeculae, osteoblasts, osteoclasts and osteocytes. The images were visualized and captured by inverted microscopy (IX71SBF2, Olympus Corporation).

To verify the osseointegration of the HHFs at the early stage, rabbits implanted with the HHFs for 1–4 weeks were killed. The joint tissues containing HHFs were fixed with 4% paraformaldehyde, and sliced into ~3-μm-thick sections using a microtome (Leica RM 2135, Leica Microsystems). For Picrosirius Red staining, the slices were stained with 0.1% Picrosirius Red solution (Head Biotechnology, 26357-02). For Masson–Goldner staining, the slices were successively stained with Goldner I (Morphisto, 25642-2), Goldner II (Morphisto, 26966-2) and Goldner III (Morphisto, 26007-11). For methylene blue–acid fuchsin staining, the slices were stained by methylene blue Solution A and B (Leagene, DB0088) to evaluate the osteoblast activity. For tartrate-resistant acid phosphatase (TRAP) staining, the slices were successively stained with TRAP dye solution (Servicebio, G1050), haematoxylin (Servicebio, G1004) and ammonia (Servicebio, G1040) to observe the amount of osteoclasts.

The immunohistochemical staining of CD31 and VEGF was performed to verify the revascularization induced by the implanted HHFs. For CD31 staining, nucleus was labelled with DAPI Fluoromount-G (Servicebio, G1012). The primary antibodies were anti-CD31 antibodies (1:200, ABclonal, A2104). The secondary antibody was anti-rabbit IgG (H + L) (1:400, Cell Signaling, 4412S). The CD31-positive vessels were stained by both DAPI and anti-CD31 antibodies (blue and green). For VEGF staining, nucleus was labelled with DAPI Fluoromount-G (Servicebio, G1012). The primary antibodies were VEGF antibodies (1:20, Invitrogen, XF3629101A) and the secondary antibody was anti-rabbit IgG (H + L) (1:400, Cell Signaling, 4412S). The VEGF-positive vessels were stained by both DAPI and VEGF antibodies (blue and red).

The immunohistochemical staining of CGRP was performed to verify the reinnervation induced by the implanted HHFs. Nucleus was

labelled with DAPI Fluoromount-G (Servicebio, G1012). The primary and secondary antibodies were CGRP antibody (1:200, ABclonal, A5542) and anti-rabbit IgG (H + L) (1:400, Cell Signaling, 4412S), respectively. The CGRP-positive nerves were stained by both DAPI and CGRP antibodies (blue and green). The resulting samples were imaged at ×20 on a Nikon C2+ microscope.

For long-term in vivo safety studies, rabbits implanted with HHFs for different durations were killed. The joint tissues containing HHFs were fixed as above. Nucleus was labelled with DAPI Fluoromount-G (Servicebio, G1012) and sections were stained using an H&E staining kit (Servicebio, G1005) and a Masson's trichrome staining kit (Servicebio, G1006). For immunohistochemical staining, the primary antibodies were F4/80 antibodies (Servicebio, GB11027) and secondary antibody was Cy3-conjugated goat anti-rabbit IgG (H + L) (Servicebio, GB25303).

For TEM characterization, fresh organs were fixed with 2.5% glutaraldehyde for 12 h and successively dehydrated using 30%, 50%, 70%, 80%, 90%, 95% and 100% ethanol for 15 min. After embedding in epoxy resin, the organs were sliced into ~80-nm-thick sections using a microtome (Leica EM UC7, Leica Microsystems). The sections were subsequently stained with lead citrate solution and uranyl acetate for 5–10 min, and finally dried for TEM observation (JEM-2100F, JEOL).

Enzyme-linked immunosorbent assay

At 4 and 13 weeks after implantation of HHFs, blood samples from the rabbits were collected and stored at 4 °C for 24 h before use. Serum was obtained by centrifuging the blood sample at 3,000*g* for 15 min. Concentrations of alanine aminotransferase, interleukin-1, tumour necrosis factor-α and interferon-β were measured by enzyme-linked immunosorbent assay kits (Shanghai Enzyme-linked Biotechnology).

Transcriptome sequencing, proteomics sequencing and data analysis

For in vitro experiments, MSCs (1×10^6 cells) were cultured on helical PET fibres and HHFs for 6 h, 1 day, 3 days and 5 days before the cells were isolated for proteomic analysis. MSCs (1×10^6 cells) were cultured on carbon plates, helical carbon fibres, HHFs and PET plates, helical PET fibres, and hierarchical helical PET fibres for proteomic and transcriptomic analysis. For in vivo experiments, HHF and PET fibres were implanted into rabbits for 2 weeks and the bone surrounding the implants was collected for proteomic analysis. We used a fast-sequence proteomic workflow[52] to identify 7,321 proteins with a 1% protein false discovery rate. The differentially expressed proteins (two-tailed unpaired Student's *t*-test, $P < 0.05$) at each time point for both the HHF and PET fibre groups were subsequently screened through the Gene Ontology (GO) and Kyoto Encyclopedia of Genes and Genomes (KEGG) databases to identify the underlying signalling pathways that are activated by either topographic features or chemical components of HHFs.

RNA-seq data analysis. For transcriptome sequencing, MSCs were treated with Trizol reagent (Beyotime Biotechnology, R0016) and stored at −80 °C before sequencing. RNA was extracted from cells according to the reagent protocols. For library preparation of RNA sequencing, a total of 500 ng RNA per sample was used as the input material for the RNA sample preparations. Sequencing libraries were generated using Ribo-off rRNA Depletion Kit (H/M/R) (Vazyme N406-02) and VAHTS Universal V6 RNA-seq Library Prep Kit for Illumina (Vazyme, NR604) following the manufacturer's recommendations. Index codes were added to attribute sequences to each sample. Transcriptome sequencing was performed using Illumina HiSeq X10 (Illumina). For quantification, the relative abundance of the transcript was measured by a normalized metric, FPKM (fragments per kilobase of transcript per million mapped reads). For further analysis, transcripts with an FPKM score >1 were retained.

Liquid chromatography–tandem mass spectrometry. Digested peptides were analysed on a Q-Exactive HFX (Thermo Fisher Scientific) interfaced with an Easy-nLC 1200 nanoflow LC system (Thermo Fisher Scientific). Peptide samples were redissolved with 0.1% formic acid (Sigma, F0507) in water and loaded onto a homemade trap column (100 µm × 2 cm; pore size, 120 Å; particle size, 3 µm; SunChrom), separated by a homemade silica microcolumn (150 µm × 30 cm; pore size, 120 Å; particle size, 1.9 µm; SunChrom). A 150 min gradient of 4–100% mobile phase B (80% acetonitrile, Honeywell, 34967; 0.1% formic acid) at a flow rate of 600 nl min^{-1} was used. The protein quantification consisted of an MS1 scan at a resolution of 120,000 (at 200 *m*/*z*) with an automated gain control value of 3×10^6, a maximum injection time of 80 ms and a scan range from *m*/*z* 300 to 1,400. The Top60 precursor ions from MS1 were selected for MS2 scans with higher-energy collision dissociation detected in the Orbitrap first (*R* (resolution) = 7,500 at 200 *m*/*z*; automated gain control target, 5×10^4; maximum injection time, 20 ms; isolation window, 1.6 *m*/*z*; normalized collision energy, 27%; dynamic exclusion of previously acquired precursor ions was enabled at 12 s). MS raw files generated by liquid chromatography–tandem mass spectrometry were processed with the proteomics cloud platform Firmiana[53] using the Mascot v.2.4 search engine against the human NCBI reference proteome database. For each identified peptide, the extracted-ion chromatogram (XIC) was extracted by searching against MS1 based on its identification information, and then the abundance was estimated by calculating the area under the extracted extracted-ion chromatogram curve. As for protein abundance calculation, the non-redundant peptide list was applied to assemble proteins according to the parsimony principle. Finally, a traditional label-free, intensity-based absolute quantification (iBAQ) algorithm was used to estimate protein abundance, which divided the protein abundance (derived from the intensities of identified peptides) by the number of theoretically observable peptides.

Pathway enrichment analysis. Pathway enrichment analysis was performed by DAVID (https://david.ncifcrf.gov/) and ConsensusPathDB (http://cpdb.molgen.mpg.de/CPDB). The *P* value is calculated based on the hypergeometric distribution and the significant pathway ($P < 0.05$) was used for further study.

ACL reconstruction on sheep in vivo

The sheep experiments were approved by the Institutional Animal Care and Use Committee at Fudan University and the Institutional Animal Care and Use Committee of Shanghai Jiao Tong University Animal Department (number PLJC20-0078-1). All animals were housed at the animal care laboratory at the College of Pharmacy in accordance with the regulations set by the National Institutes of Health.

Nine healthy adult Chinese Hu sheep (seven males, 2 years old, weighing 52.3–55.4 kg) were selected. The ACL reconstruction procedure was performed on the right knee under general anaesthesia. A medial arthrotomy was performed, and patella was laterally displaced. The fat pad was partially excised to expose the ACL. The knee joint was then flexed to 140°. The native ACL was carefully resected by using a scalpel. A femoral and tibial tunnel was positioned and drilled at the centre of the ACL anatomic footprint inside out by using K-wire with a diameter of 2 mm. Then, the bone tunnels were further dilated to 5.0 mm (Supplementary Fig. 21a). A guiding suture loop was first passed through the tibial and femoral tunnel (Supplementary Fig. 21b). Two strands of HHFs (diameter, ~2 mm) were then passed through the tunnel and fixed by an adjustable-loop cortical suspension device (GraftLoop, Ligatech) at the femoral side and a screw at the tibial side (Supplementary Figs. 21c,d and 22). The HHFs were tensioned with 30 knee flexion–extension cycles so that no obvious graft–tunnel motion was observed. At the tibial side, the HHFs were tied with a surgical knot and reinforced with one additional square knot (Supplementary Fig. 21e). After fixation, the ligament knot was sutured

with surrounding tissue. The knee joint was flushed with saline and the wound was sutured layer by layer. After surgery, the sheep were allowed free activity in separated cages and were well taken care of. The wounds were inspected and disinfected every 3 days and the sutures were removed after 14 days. The gait of the sheep was also evaluated postoperatively.

Evaluation of ACL reconstruction in the sheep model

The sheep were killed after 13 weeks, 9 months and 21 months postoperatively. The articular capsule was cut open and articular cavity was exposed for morphology evaluation. The knees, including femur and tibia, were dissected for further testing. The specimens were first fixed in neutral formalin liquid with a concentration of 10% for the follow-up histological examination.

The CT scanning (Toshiba Aquilion Prime) of tibia was conducted with a slice thickness of 0.6 mm. Images were acquired at 140 kV with a scanning baseline of B40S. Three-dimensional CT image reconstruction was performed with a Vitrea imaging workstation (Vital Images). The plane parallel to the longitudinal axis of the femoral bone tunnel was reconstructed using a multiplanar reformation technique. Femoral tunnel diameters at aperture, midpoint and exit, and the maximal tunnel diameter in the femoral side, were measured with a DICOM Viewer (Vitrea, v.6.7.1). The femoral tunnel midpoint was defined as the midpoint between aperture and exit along the longitudinal tunnel axis. For the histological examination, an uncalcified tibial bone block containing complete bone tunnel were embedded in polymethyl methacrylate. By using a hard tissue section method, the bone block was sectioned into 10-μm-thick slices at the middle point of the tunnel and along the direction parallel to the longitudinal axis of the bone tunnels. The intraosseous portions were then stained with H&E and Picrosirius Red dye, respectively. A panorama of the femoral tunnel was produced by ZEN 3.0 software (Zeiss) to observe the histological morphology of graft and graft–bone interface.

Statistics and reproducibility

Statistical analysis was performent with Graphpad Prism 9.0 and Microsoft Excel 2016. The results are expressed as mean ± s.d. The statistical differences between two groups and among multiple groups were analysed using unpaired two-tailed *t*-test and one-way analysis of variance, respectively. *P* values: n.s., not significant ($P > 0.05$), $^{*}P < 0.05$, $^{**}P < 0.01$, $^{***}P < 0.005$ and $^{****}P < 0.001$). Experiments in Fig. 1b–f, Supplementary Figs. 1a,b, 8, 12, 18a and 19a, and Extended Data Figs. 1i–k, 2e,f, 5e,f, 8c and 9d,f were repeated three times with distinct samples. Experiments in Figs. 3g–j,l and 5b,c and Extended Data Fig. 3a–c were repeated four times with distinct samples. Experiments in Supplementary Figs. 4, 13, 14, 15, 16 and 17 and Extended Data Figs. 2a–d, 5b,c, 6a–e and 7b,c were repeated twice with distinct samples.

Reporting summary

Further information on research design is available in the Nature Portfolio Reporting Summary linked to this article.

Data availability

Source data are available for Figs. 2 and 3 and Extended Data Figs. 1, 2, 4 and 5 in the associated source data files. The transcriptomics raw data have been deposited in NODE (https://www.biosino.org/node) under accession number OEP002944. All raw data of mass spectrum have been deposited to the ProteomeXchange Consortium (http://proteomecentral.proteomexchange.org) via the iProX partner repository with the dataset identifier PXD032128. Source data are provided with this paper.

References

52. Ding, C. et al. A fast workflow for identification and quantification of proteomes. *Mol. Cell Proteom.* **12**, 2370–2380 (2013).
53. Feng, J. W. et al. Firmiana: towards a one-stop proteomic cloud platform for data processing and analysis. *Nat. Biotech.* **35**, 409–412 (2017).

Acknowledgements

We thank P. Liu of NAMSA China for support with the sheep experiment, Q. Jin and H. Zhou of Shanghai Institute of Traumatology & Orthopaedics for technical support with the histology preparation, Y. Xu of Fudan University, C. Liu of Shanghai University, Z. Nie of Fudan University and K. Lv of Xinhua Hospital Affiliated to Shanghai Jiao Tong University School of Medicine for insightful discussions and suggestions, and A.L. Chun of Science Storylab for critically reading and editing the manuscript. This work was supported by the Science and Technology Commission of Shanghai Municipality 20JC1414902 (H.P.), 21511104900 (H.P.), 19441901600 (S.C.), 19441902000 (S.C.); the National Natural Science Foundation of China 22175042 (P.C.), T2222005 (P.C.), 52122310 (X.S.), 22075050 (X.S.), 81572108 (S.C.), 81772339 (S.C.), 11872150 (F.X.), 12122204 (F.X.), 31770886 (C.D.), 31972933 (C.D.), 31700682 (C.D.); the Ministry of Science and Technology of the People's Republic of China 2017YFA0505102 (C.D.), 2020YFE0201600 (C.D.), 2022YFA1303200 (C.D.); the Shanghai Shuguang Program 21SG05 (F.X.), 19SG02 (C.D.); and the Shanghai Sailing Program 20YF1404500 (L.L.).

Author contributions

Conceptualization: H.P., P.C., X.S. Materials preparation: Y.X., T.Z., H.Y., S.X., L.L., L.W. Animal experiments: F.W., L.W., T.Z., S.X., Y.X. Cell experiments: S.X., J.G., X.Y., H.Y. Transcriptomic and proteomic analysis: F.Z., J.Z., L.W. μCT and histological characterization: Y.X., F.W., S.X. Finite-element simulation: F.X., Y.Y. Schematic diagrams and videos: L.W., C.W., X.S., T.Z. Writing—original draft: L.W., S.X., P.C., H.P., Y.X., F.W. Writing—review and editing: H.P., P.C., X.S., C.D., S.C., J.D., H.Y. Supervision: H.P., C.D., P.C., X.S., S.C.

Competing interests

The authors declare no competing interests.

Additional information

Extended data is available for this paper at https://doi.org/10.1038/s41565-023-01394-3.

Supplementary information The online version contains supplementary material available at https://doi.org/10.1038/s41565-023-01394-3.

Correspondence and requests for materials should be addressed to Shiyi Chen, Xuemei Sun, Peining Chen, Chen Ding or Huisheng Peng.

Peer review information *Nature Nanotechnology* thanks Hala Zreiqat, Georg Duda and Yunzhi Peter Yang for their contribution to the peer review of this work.

https://doi.org/10.1038/s41565-023-01394-3

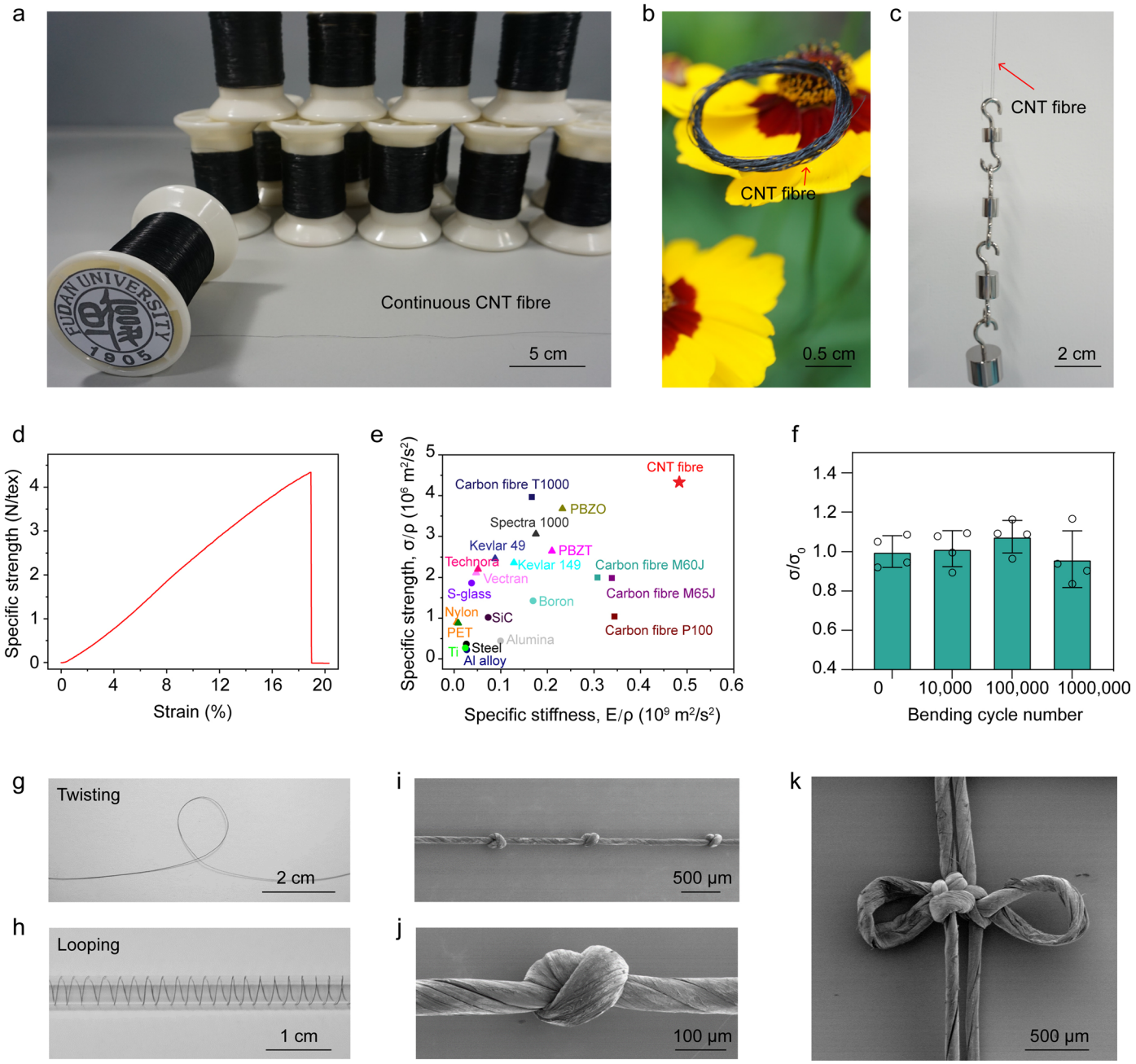

Extended Data Fig. 1 | The mechanical properties of CNT fibres. a, Photograph showing rolls of continuous CNT fibres. **b**, **c**, Photographs showing high strength and light weight of the CNT fibre, respectively. **d**, Typical specific strength-strain curve of a CNT fibre. **e**, Mechanical performance of CNT fibre compared to other fibre materials such as metals, polymers and carbon fibres. σ is breaking strength, E is Young's modulus, and ρ is density. **f**, Tensile tests performed on CNT fibres show they display stable breaking strengths (σ) after 10,000, 100,000 and 1,000,000 bending cycles. The CNT fibres with length of 1 cm are bent with a curvature radius of 0.247 cm. Tensile tests are performed (with an initial applied stress of 0 MPa) by changing the displacement to determine the breaking strength (σ) of the CNT fibres. Breaking strength after bending is normalized to breaking strength before bending (σ_0). n = 4 independent samples. Each point represents an independent measurement. All data are expressed as mean ± s.d. **g**, **h**, Photographs showing high flexibility of the CNT fibre under twisting (**g**) and looping (**h**). **i**, **j**, SEM images of a knotted CNT fibre at low and high magnifications, respectively. **k**, A Chinese knot formed by the CNT fibre.

https://doi.org/10.1038/s41565-023-01394-3

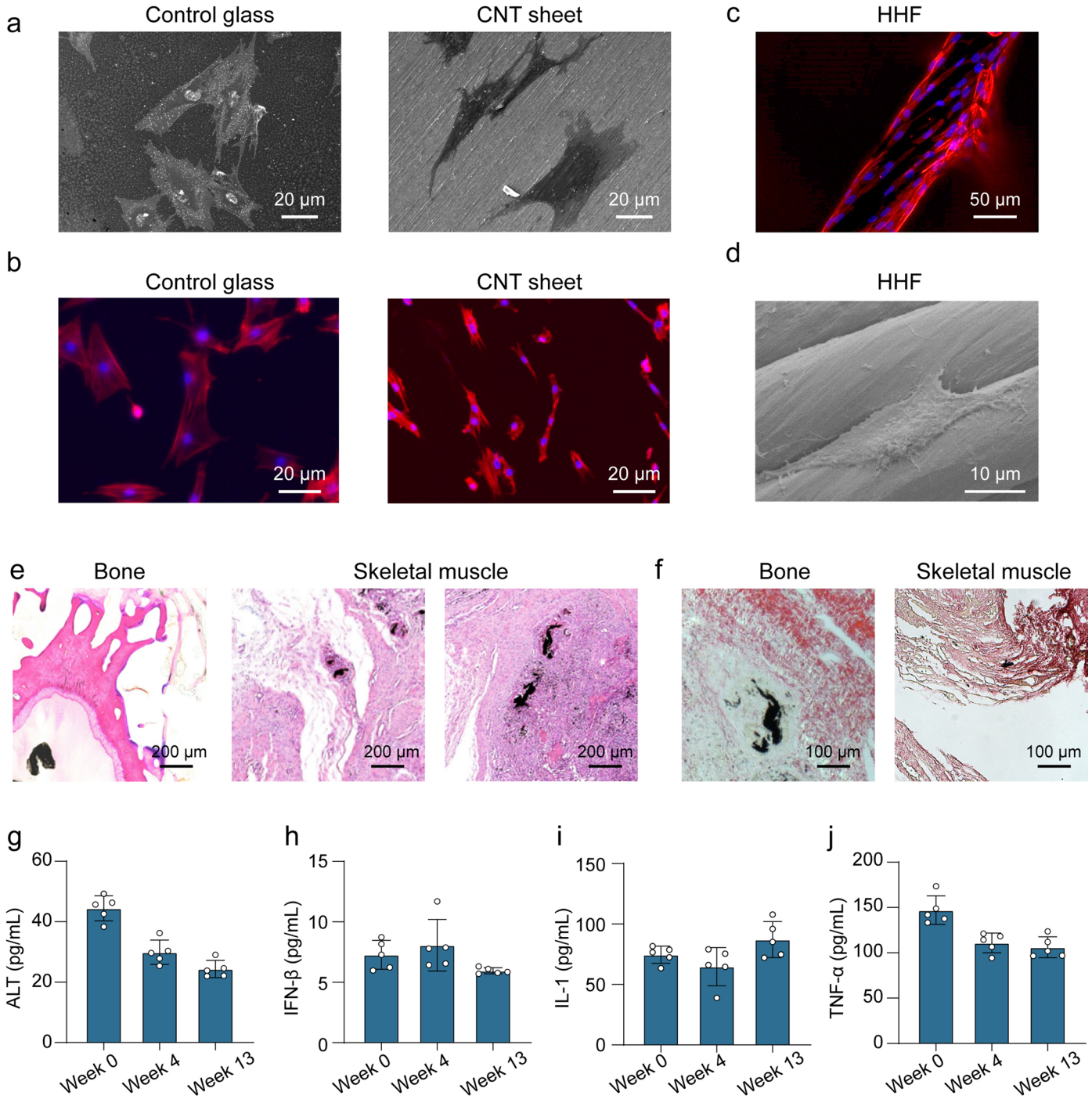

Extended Data Fig. 2 | The biocompatibility of HHF. a, SEM images of MSCs cultured on the control glass group and CNT sheets for 5 days. **b**, F-actin labelled immunostaining images of the control glass group and CNT sheets after culturing MSCs for 5 days. Red: F-actin; blue: cell nucleus. **c**, **d**, F-actin labelled immunostaining image (**c**) and SEM image (**d**) of HHF after culturing MSCs for 5 days. Red: F-actin; blue: cell nucleus. **e**, **f**, H&E (**e**) and picrosirius red (**f**) staining show HHF graft integrates well with bone and skeletal muscle after HHF implanted in rabbits for 13 weeks. **g**-**j**, Concentrations of typical plasma markers in rabbit serum after HHF implantation, showing the high biocompatibility of HHF in molecular level. Alanine aminotransferase (ALT) (**g**), interferon-β (IFN-β) (**h**), interleukin-1 (IL-1) (**i**), and tumour-necrosis factor-α (TNF-α) (**j**) concentrations varied within their normal physiological ranges. Concentrations of plasma markers are determined using enzyme-linked immunosorbent assay. Each point represents the concentration of plasma markers in each rabbit. n = 5 biologically independent experiments for each group. All data are expressed as mean ± s.d.

https://doi.org/10.1038/s41565-023-01394-3

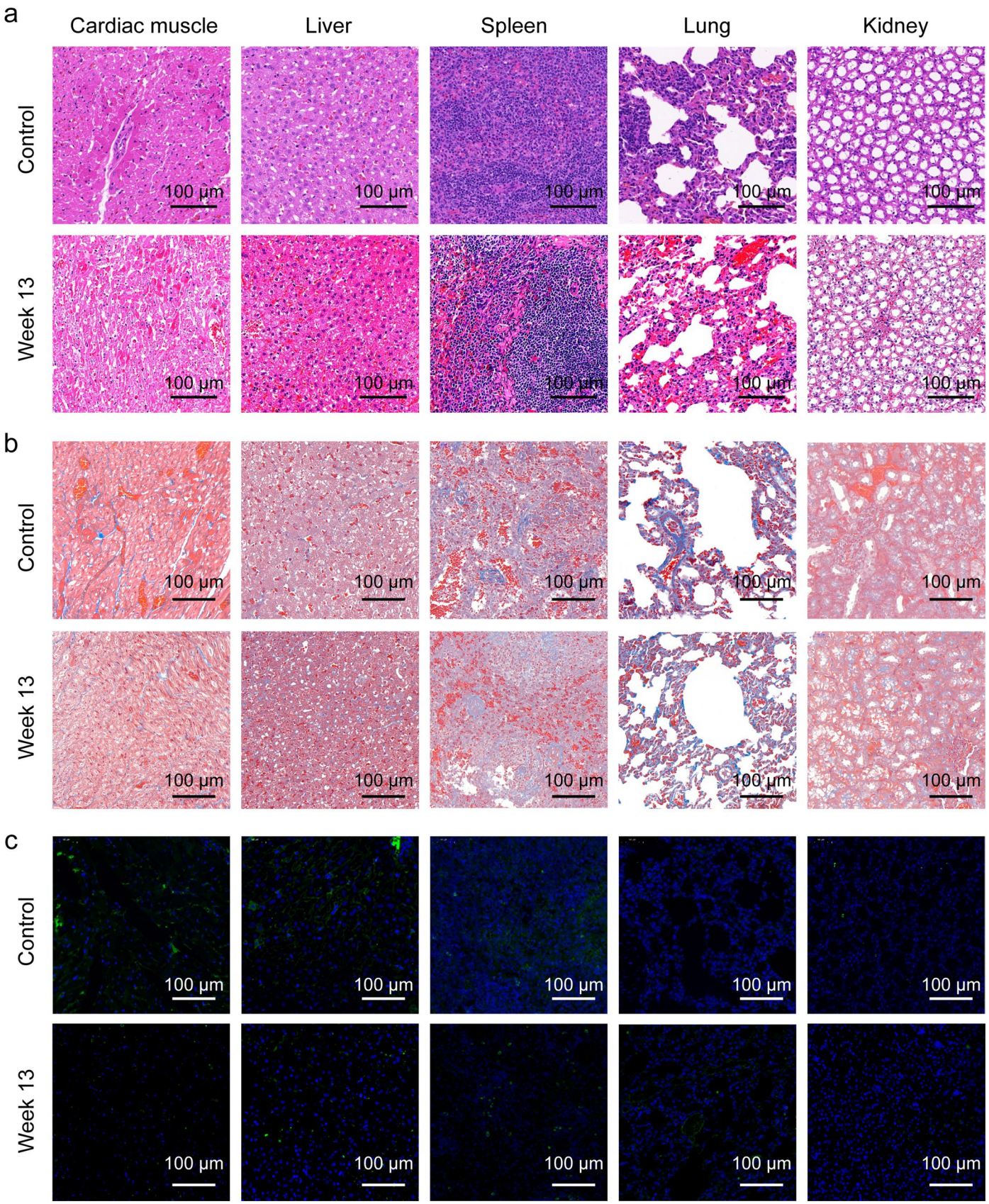

Extended Data Fig. 3 | See next page for caption.

https://doi.org/10.1038/s41565-023-01394-3

Extended Data Fig. 3 | Histological analysis to show high structural stability of HHF graft *in vivo*. **a**, H&E sections of cardiac muscle, liver, spleen, lung and kidney after 13 weeks of HHF implantation show no CNT residues. Control: rabbits without HHF. **b**, Masson's trichrome-stained tissue sections of cardiac muscle, liver, spleen, lung and kidney after 13 weeks of HHF implantation do not show any collagen deposition and peribronchial lymphocyte aggregation in any of the organs. Control: rabbits without HHF. Red: cytoplasm, muscle and erythrocytes; blue: collagen. **c**, F4/80 immunostaining of cardiac muscle, liver, spleen, lung and kidney after HHF implanted in rabbits for 13 weeks do not show any inflammatory cell infiltration in any of the organs. Control: rabbits without HHF. Nucleus is stained with DAPI (blue); inflammatory cells are stained by both DAPI and F4/80 antibodies (blue and green).

https://doi.org/10.1038/s41565-023-01394-3

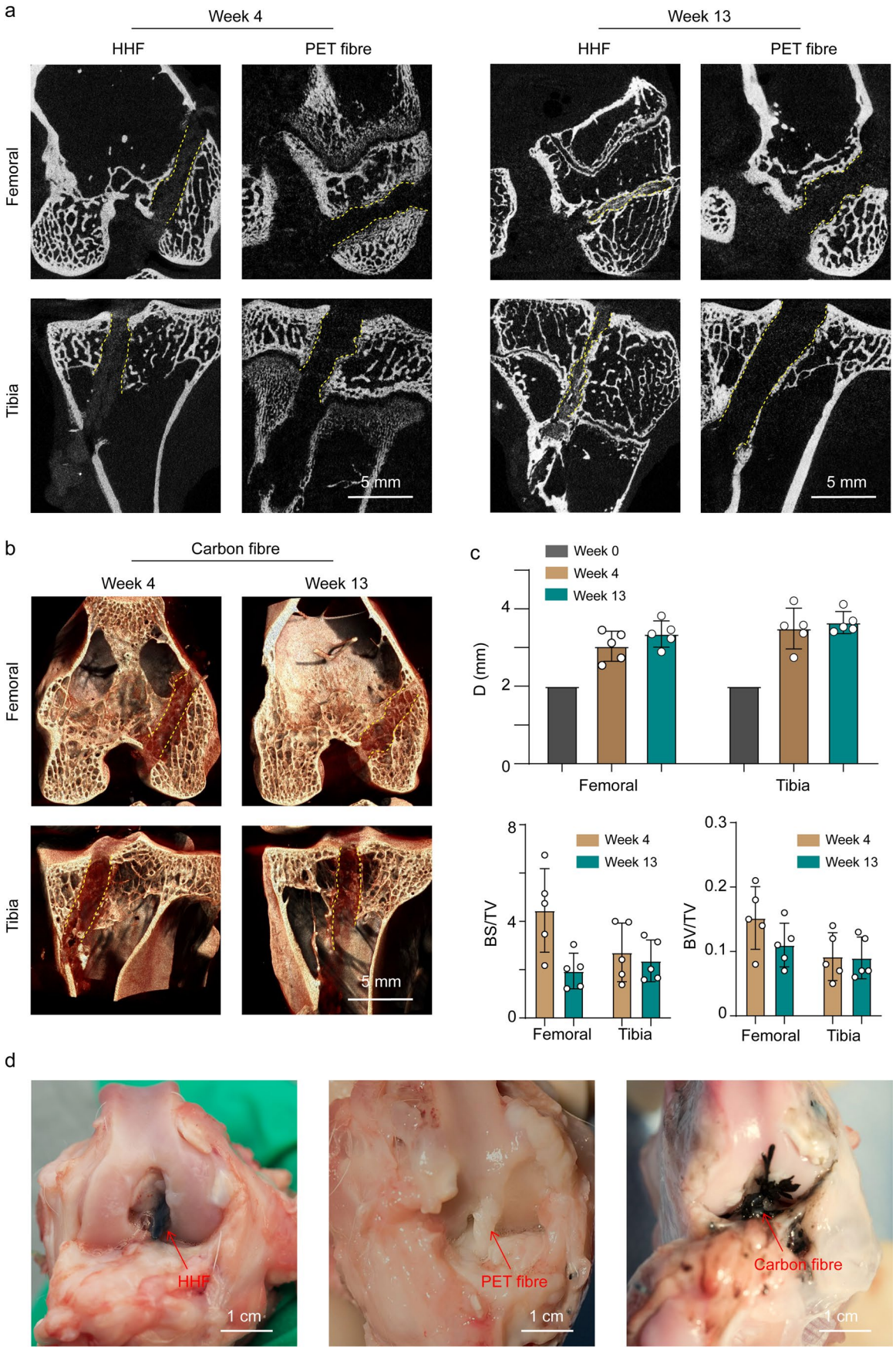

Extended Data Fig. 4 | See next page for caption.

https://doi.org/10.1038/s41565-023-01394-3

Extended Data Fig. 4 | ACL reconstruction using HHFs and controls in a rabbit model. a, μCT images of the femur and tibia of rabbits after surgery for 4 and 13 weeks with HHF and PET fibres as the ACL grafts. **b**, Three-dimensional images rebuilt from μCT data of the femur and tibia of rabbits after the surgery for 4 and 13 weeks with carbon fibres as the ACL graft. **c**, Average diameters, ratios of bone surface (BS) to total volume (TV) and bone volume (BV) to TV of femoral and tibia tunnels of rabbits after implanting carbon fibres for 4 and 13 weeks. n = 5 biologically independent experiments for each group. All data are expressed as mean ± s.d. **d**, Photographs of the femur-graft-tibia complex specimens of rabbits after the surgery for 13 weeks with HHF, PET fibres and carbon fibres as the ACL grafts.

https://doi.org/10.1038/s41565-023-01394-3

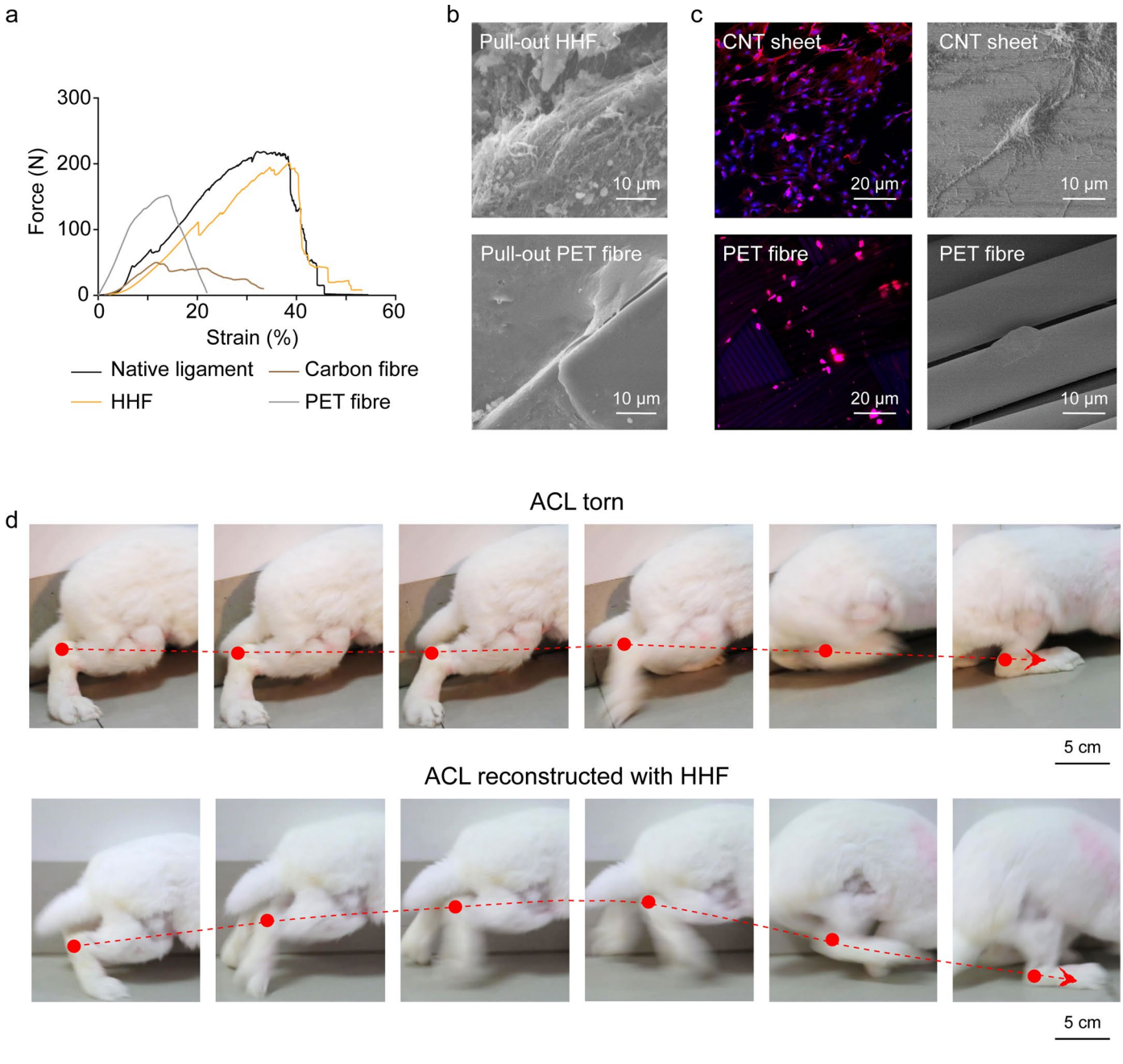

Extended Data Fig. 5 | Bio-integration of HHF grafts and controls. a, Force-strain curves of pull-out tests for native ligament, HHF, carbon fibre and PET fibre after implantation for 13 weeks. **b**, SEM images showing the surface of the pull-out HHF and PET fibre implants after 13 weeks of implantation. **c**, Immunostaining and SEM images of osteoblasts cultured on the CNT sheets and PET fibres for 5 days, respectively. **d**, Photographs showing the moving trial of the right hindleg with ACL torn (up) and reconstructed using the grafts of HHF (below) during one hopping process. **e**, H&E staining of the bone tunnel after the surgery for 13 weeks with PET fibre and carbon fibre as the ACL graft. **f**, Picrosirius-red-stained slices of bone tunnel implanted with carbon fibre under bright field (left) and polarized light (right) show almost no collagen at the carbon fibre/host bone interface.

https://doi.org/10.1038/s41565-023-01394-3

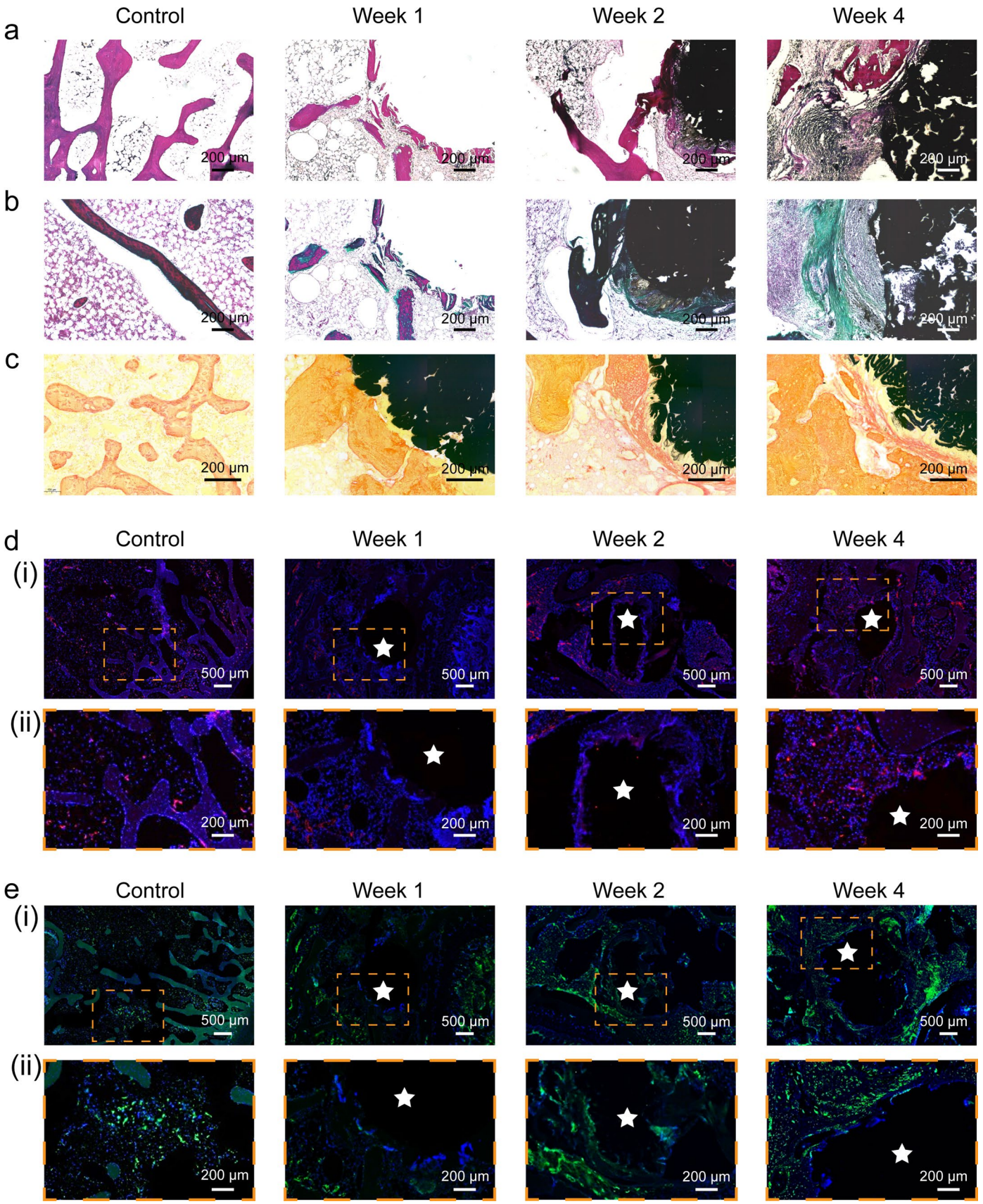

Extended Data Fig. 6 | See next page for caption.

https://doi.org/10.1038/s41565-023-01394-3

Extended Data Fig. 6 | Histological analysis to show the activity of osteoblasts, re-established crimp, re-vascularization and re-innervation induced by HHF implanted in rabbits. a, Methylene blue-acid fuchsin-stained slices of bone tunnel after HHF implantation in rabbits. Dark blue: osteoblasts; purple grey: osteoid tissue; red: newly formed bone. **b**, Masson Goldner-stained slices of bone tunnel after HHF implantation in rabbits. Red: mature bone; green: collagen; red-green: newly formed bone. **c**, Picrosirius-red-stained slices of bone tunnel implanted with HHF under bright field. Collagen tissues are gradually formed at the interfacial region between HHF and host bone from Week 1 to Week 4. **d**, (i) VEGF-stained images. Nucleus is stained with DAPI (blue); vessels are stained by both DAPI and VEGF antibodies (blue and red). The position of HHF is marked with white pentalpha. (ii) Magnified view of yellow box in (i) shows VEGF-positive vessels are formed at the interface of HHF/native bone. **e**, *(i)* CGRP-stained images. Nucleus is stained with DAPI (blue); nerves are stained by both DAPI and CGRP antibodies (blue and green). The position of HHF is marked with white pentalpha. (ii) Magnified view of yellow box in (i) shows CGRP-positive nerves are formed at the interface of HHF/native bone.

https://doi.org/10.1038/s41565-023-01394-3

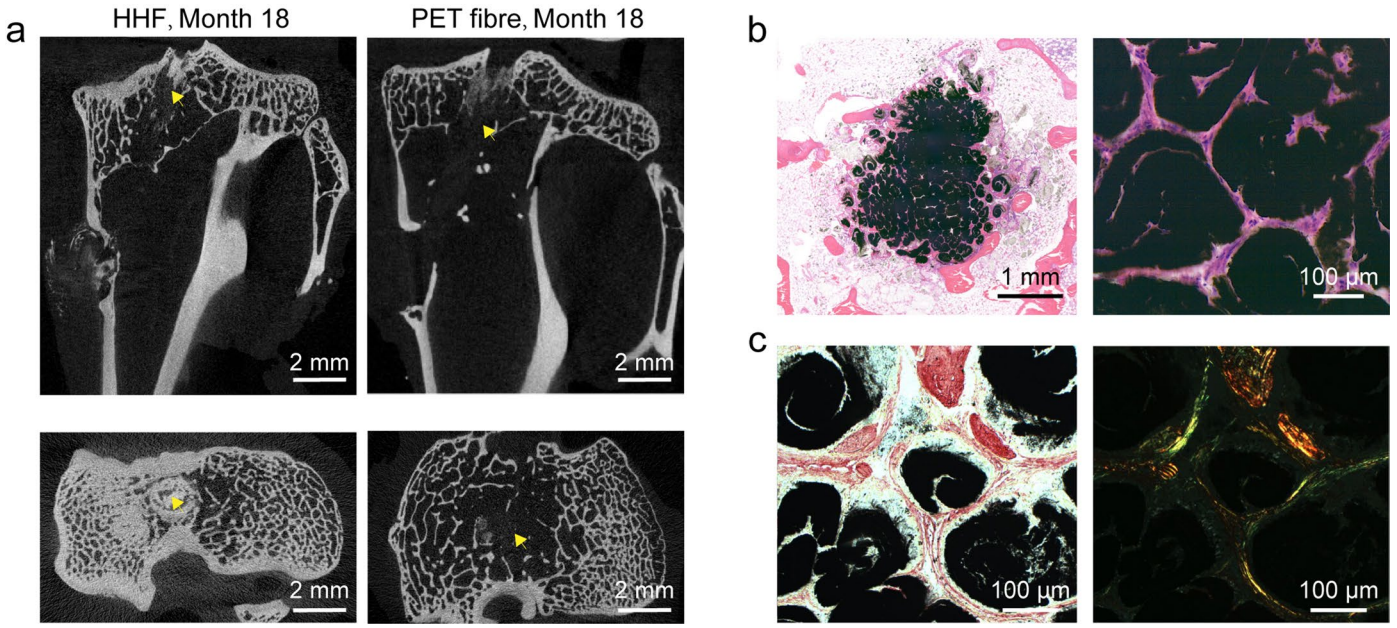

Extended Data Fig. 7 | ACL reconstruction in a rabbit model after 18 months of HHFs and PET fibres implantation. a, μCT images showing a coronal section of a femoral tunnel (top) and an axial section of a tibial tunnel (bottom, yellow arrow) after 18 months of HHF and PET fibre implantation, showing new bone tissues are completely occupied in the tunnel between the host bone and HHF. **b**, H&E-stained images of rabbit joint section after 18 months of HHF implantation show dense tissue around HHF (black) and good integration of HHF with surrounding bone. **c**, Picrosirius-red-stained slices of rabbit joint implanted with HHF for 18 months under bright field (left) and polarized light (right) show newly formed bones inside the channels among the primary fibres of HHF. A thick layer of anisotropic collagen (green) around the primary fibres of HHF is formed.

https://doi.org/10.1038/s41565-023-01394-3

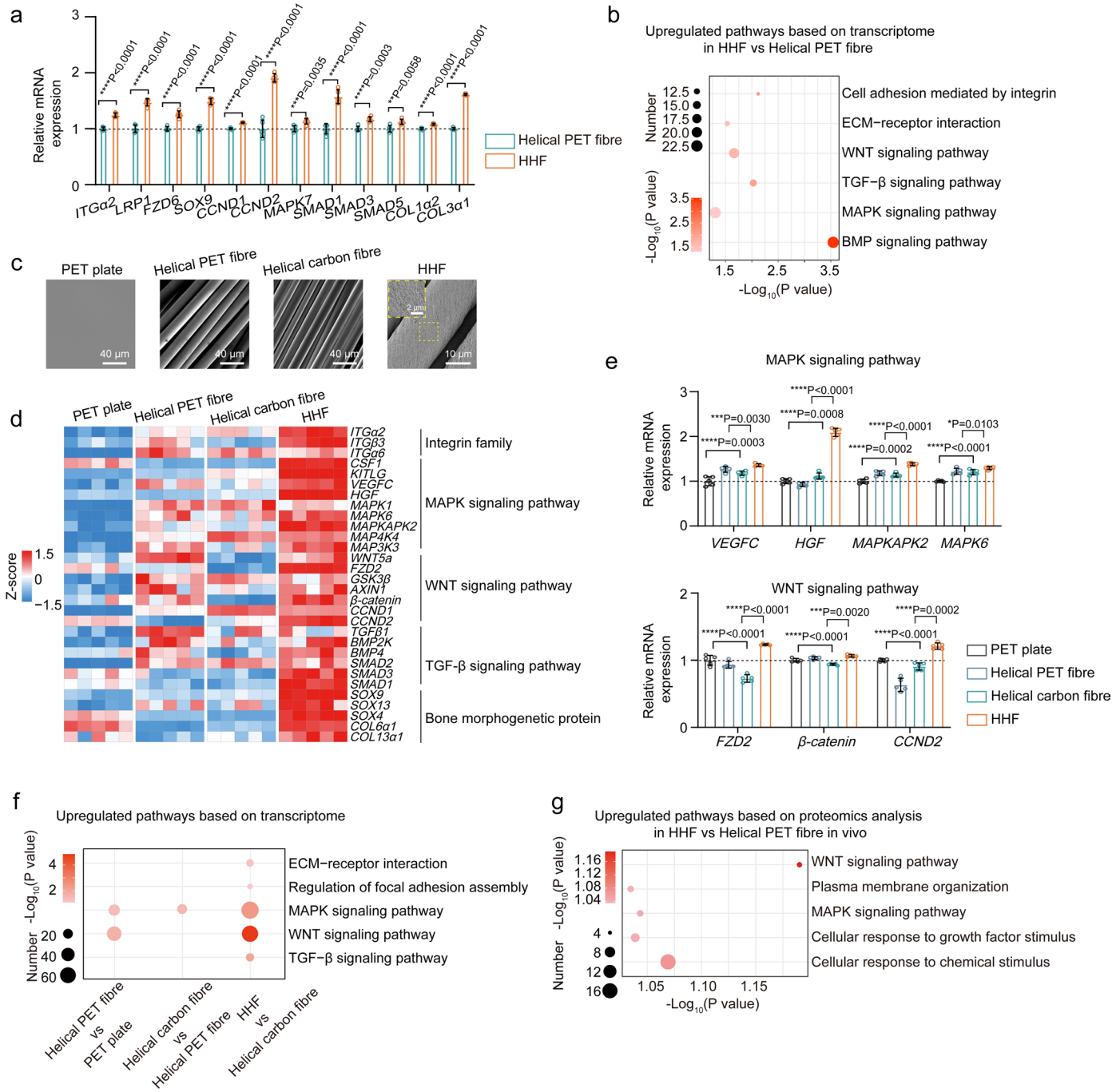

Extended Data Fig. 8 | HHF promotes osteogenesis *in vitro* and *in vivo* by activating osteogenesis-related signalling pathways. a, MSCs cultured on HHF express higher levels of typical osteogenesis-related genes than those cultured on helical PET fibre. Horizontal dotted lines represent mean of helical PET fibre group. n = 5 biologically independent experiments for each group. All data are expressed as mean ± s.d. Statistical significance was determined by unpaired two-tailed t-test (n.s., not significant, P > 0.05, *P < 0.05, **P < 0.01, ***P < 0.005 and ****P < 0.001). **b**, GO and KEGG enrichment based on transcriptomic analysis of MSCs cultured on HHF and helical PET fibre show upregulated osteogenesis-related signalling pathways. n = 5 biologically independent experiments for each group. **c**, SEM images of different substrates for MSC culturing. (i) PET plate. (ii) Helical PET fibre. (iii) Helical carbon fibre. (iv) HHF. **d**, Heatmap analysis of differentially expressed genes related to osteogenesis of MSCs cultured on PET plate, helical PET fibre, helical carbon fibre and HHF. n = 5 biologically independent experiments for each group. **e**, MSCs cultured on PET plate, helical PET fibre, helical carbon fibre and HHF express different levels of typical osteogenesis-related genes in MAPK (up) and WNT (below) signalling pathway. Horizontal dotted lines represent mean of PET plate group. n = 5 biologically independent experiments for each group. Data are expressed as mean ± s.d. Statistical significance was determined by unpaired two-tailed t-test between two groups and one-way ANOVA among multiple groups (n.s., not significant, P > 0.05, *P < 0.05, **P < 0.01, ***P < 0.005 and ****P < 0.001). **f**, GO and KEGG enrichment based on transcriptomic analysis of MSCs show upregulated osteogenesis-related signalling pathways for different pairwise comparisons (carbon component: helical carbon fibre *vs* helical PET fibre; micrometre channel: helical PET fibre *vs* PET plate; nanometre channel: HHF *vs* helical carbon fibre). n = 5 biologically independent experiments for each group. **g**, GO and KEGG enrichment based on proteomic analysis of rabbit bone implanted with HHF and helical PET fibre show osteogenesis-related signalling pathways are upregulated *in vivo*. n = 3 biologically independent experiments for each group. Pathway enrichment analysis in (**b**, **f**, **g**) was performed by DAVID (https://david.ncifcrf.gov/) and ConsensusPathDB (http://cpdb.molgen.mpg.de/CPDB), P value is calculated based on the hypergeometric distribution and the significant pathway (P value < 0.05) was used for further study.

https://doi.org/10.1038/s41565-023-01394-3

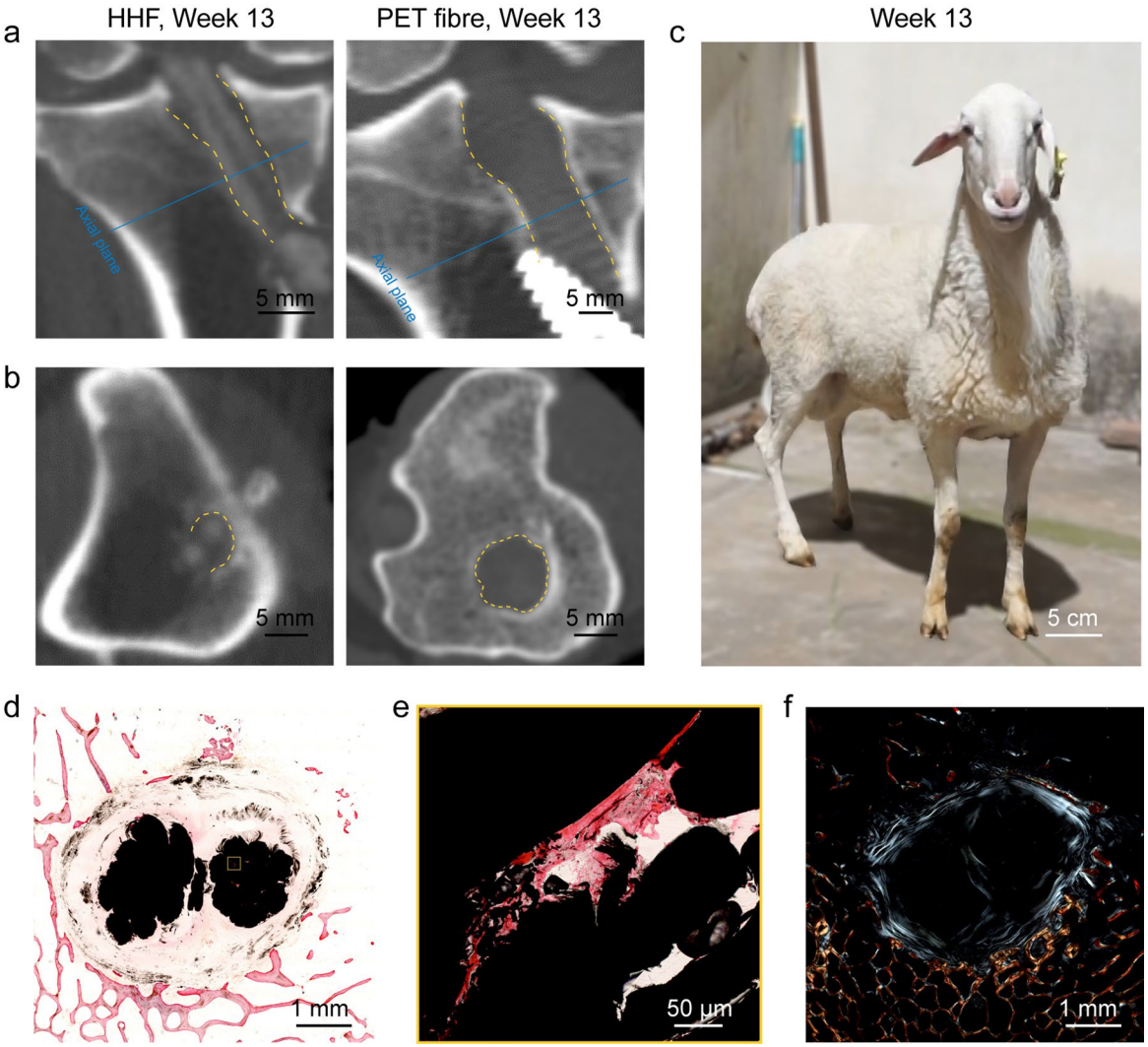

Extended Data Fig. 9 | ACL reconstruction using HHF graft restores mobility in a large animal model of sheep. a, CT images of tibias in a coronal plane using HHFs and PET fibres as grafts after surgery for 13 weeks. The tunnels are marked with yellow dashed lines. **b**, CT images of the tibia scanned in axial plane at the position marked with blue lines in (**a**). **c**, Photograph of the postoperative sheep standing with a normal gait in Week 13. **d**, H&E-stained image of the tibial tunnels after 13 weeks of implanting HHFs. **e**, Enlarged view of yellow box marked in (**d**). The newly-formed bone tissues are observed in the channels within the HHF. **f**, Picrosirius-red-stained slices of the bone tunnels after implanting HHFs for 13 weeks.

nature portfolio

Corresponding author(s): Shiyi Chen, Xuemei Sun, Peining Chen, Chen Ding, Huisheng Peng

Last updated by author(s): May 14, 2022

Reporting Summary

Nature Portfolio wishes to improve the reproducibility of the work that we publish. This form provides structure for consistency and transparency in reporting. For further information on Nature Portfolio policies, see our Editorial Policies and the Editorial Policy Checklist.

Statistics

For all statistical analyses, confirm that the following items are present in the figure legend, table legend, main text, or Methods section.

n/a	Confirmed
☐	☒ The exact sample size (*n*) for each experimental group/condition, given as a discrete number and unit of measurement
☐	☒ A statement on whether measurements were taken from distinct samples or whether the same sample was measured repeatedly
☐	☒ The statistical test(s) used AND whether they are one- or two-sided *Only common tests should be described solely by name; describe more complex techniques in the Methods section.*
☒	☐ A description of all covariates tested
☒	☐ A description of any assumptions or corrections, such as tests of normality and adjustment for multiple comparisons
☐	☒ A full description of the statistical parameters including central tendency (e.g. means) or other basic estimates (e.g. regression coefficient) AND variation (e.g. standard deviation) or associated estimates of uncertainty (e.g. confidence intervals)
☐	☒ For null hypothesis testing, the test statistic (e.g. *F*, *t*, *r*) with confidence intervals, effect sizes, degrees of freedom and *P* value noted *Give P values as exact values whenever suitable.*
☒	☐ For Bayesian analysis, information on the choice of priors and Markov chain Monte Carlo settings
☒	☐ For hierarchical and complex designs, identification of the appropriate level for tests and full reporting of outcomes
☒	☐ Estimates of effect sizes (e.g. Cohen's *d*, Pearson's *r*), indicating how they were calculated

Our web collection on statistics for biologists contains articles on many of the points above.

Software and code

Policy information about availability of computer code

Data collection	Tensile machine (TA Instruments-Waters LLC ElectroForce 3220), Ultraviolet-visible spectrometer (Perkin-Elmer Lambda750), Nikon C2+, Transmission electron microscopy (JEM-2100F, JEOL, Ltd.), Digital single lens-reflex camera (5D Mark IV, Canon Inc.) with a macro lens (EF 100 mm 2.8L IS macro, Canon Inc.), Micro-computed tomography for rabbits (SkyScan 1176, BRUKER), Micro-computed tomography for sheep (Toshiba Aquilion Prime), Inverted microscopy (IX71SBF2, Olympus Corporation), Raman (Renishaw, NTEGRA Spectra II), Q Exactive HF-X mass spectrometer (Thermo Fisher Scientific), Easy-nLC 1200 nanoflow LC system (Thermo Fisher Scientific), Illumina HiSeq X10 (Illumina, USA), Electronic universal material testing system (AGS-X, Shimadzu, Co.), EXAKT 510 dehydration system (EXAKT Technologies Inc.), Microtome (Leica RM 2135, Leica Microsystems), Illumina HiSeq X10 (Illumina, USA)
Data analysis	The micro-computed tomography images of femur-graft-tibia complexes of rabbits were analyzed and processed into 3D models via the CTVox (BRUKER, V1.6.4.0) to analyze the longitudinal section of the femoral and tibial tunnel. The panorama of femoral tunnel of sheep was produced by ZEN 3.0 software (ZEISS) to observe the histological morphology of graft and graft-bone interface. Femoral tunnel diameters at aperture, midpoint, exit as well as the maximal tunnel diameter of sheep were measured through DICOM Viewer (Vitrea, V6.7.1). The von Mises stress distribution along the fibre model was simulated using the ABAQUS software 6.13. The mass spectrometry raw files were processed in Firmiana, searched against human National Center for Biotechnology Information (NCBI) RefSeq protein database using Mascot 2.4 (Matrix Science Inc, London, UK). The data analysis was conducted using Graphpad Prism 9.0 and Microsoft Excel 2016.

For manuscripts utilizing custom algorithms or software that are central to the research but not yet described in published literature, software must be made available to editors and reviewers. We strongly encourage code deposition in a community repository (e.g. GitHub). See the Nature Portfolio guidelines for submitting code & software for further information.

Data

Policy information about availability of data

All manuscripts must include a data availability statement. This statement should provide the following information, where applicable:

- Accession codes, unique identifiers, or web links for publicly available datasets
- A description of any restrictions on data availability
- For clinical datasets or third party data, please ensure that the statement adheres to our policy

The mass spectrometry raw files were processed in Firmiana, searched against human National Center for Biotechnology Information (NCBI) RefSeq protein database using Mascot 2.4 (Matrix Science Inc, London, UK). For mRNA quantification, the relative abundance of the transcript was measured by a normalized metric, FPKM (Fragments Per Kilobase of transcript per Million mapped reads). Pathway enrichment analysis was performed by DAVID (https://david.ncifcrf.gov/) and ConsensusPathDB (http://cpdb.molgen.mpg.de/CPDB).

The transcriptomics raw data have been deposited in NODE (https://www.biosino.org/node) under the accession number OEP002944.
All raw data of mass spectrum have been deposited to the ProteomeXchange Consortium (http://proteomecentral.proteomexchange.org) via the iProX partner repository with the dataset identifier PXD032128.

Field-specific reporting

Please select the one below that is the best fit for your research. If you are not sure, read the appropriate sections before making your selection.

☒ Life sciences ☐ Behavioural & social sciences ☐ Ecological, evolutionary & environmental sciences

For a reference copy of the document with all sections, see nature.com/documents/nr-reporting-summary-flat.pdf

Life sciences study design

All studies must disclose on these points even when the disclosure is negative.

Sample size	Sample sizes were provided in the Methods section or figure legends for each experiment. No statistical method was used to predetermine the sample size for each study. The sample sizes were chosen on the basis of the previous similar works (Knee Surg. Sport Tr. A. 2021, 29, 3678; Orthop. J. Sports. Med, 2021, 9, 663), that help us to observe reliable and reproducible conclusions.
Data exclusions	No data were excluded from this study.
Replication	All experiments were reliably reproduced and all conclusions were reproducible from these experiments. Details of experimental replicates are given in the figure legends.
Randomization	All the animals, cells and samples were randomly allocated to the experimental group and the control group.
Blinding	Blinding was not performed, because there was no subjective test in this study.

Reporting for specific materials, systems and methods

We require information from authors about some types of materials, experimental systems and methods used in many studies. Here, indicate whether each material, system or method listed is relevant to your study. If you are not sure if a list item applies to your research, read the appropriate section before selecting a response.

Materials & experimental systems

n/a	Involved in the study
☐	☒ Antibodies
☐	☒ Eukaryotic cell lines
☒	☐ Palaeontology and archaeology
☐	☒ Animals and other organisms
☒	☐ Human research participants
☒	☐ Clinical data
☒	☐ Dual use research of concern

Methods

n/a	Involved in the study
☒	☐ ChIP-seq
☒	☐ Flow cytometry
☒	☐ MRI-based neuroimaging

Antibodies

Antibodies used	Primary mouse anti-F-actin (1:200, Abcam, ab205), Alexa Fluro 488 goat anti-mouse IG (H+L)(1:400, Life Technologies, A11001),

Antibodies used	Alexa Fluro 647 goat anti-mouse IG (H+L) (1:400, Life Technologies, A21235), F4/80 antibodies (1:500, GB11027, Servicebio), Cy3-conjugated goat anti-rabbit IgG (H+L) (1:400, GB25303, Servicebio), anti-CD31 antibodies (1:200, ABclonal, A2104), anti-rabbit IgG (H+L) (1:400, Cell Signaling, 4412S), VEGF antibodies (1:20, Invitrogen, XF3629101A), CGRP antibody (1:200, ABclonal, A5542)
Validation	All antibodies were well-recognized in the field and were verified by the supplier. The validation statements can be found on their manufactures' websites as below: Primary mouse anti-F-actin (1:200, Abcam, ab205): https://www.abcam.cn/f-actin-antibody-nh3-ab205.html F4/80 antibodies (1:500, GB11027, Servicebio): https://www.servicebio.cn/goodsdetail?id=1330 anti-CD31 antibodies (1:200, ABclonal, A2104): https://abclonal.com.cn/catalog/A2104 VEGF antibodies (1:20, Invitrogen, XF3629101A): https://assets.thermofisher.cn/TFS-Assets/LSG/certificate/Certificates-of-Analysis/MA513182_XF3629101A.PDF CGRP antibody (1:200, ABclonal, A5542): https://abclonal.com.cn/catalog/A5542

Eukaryotic cell lines

Policy information about cell lines

Cell line source(s)	Mesenchymal stem cells (SCSP-405) were obtained from Cell Bank of Shanghai, Chinese Academy of Sciences (Shanghai, China).
Authentication	The cell lines are certified by the manufacturers (i.e. morphology) and maintained with selection medium according to manufacturer's suggestion.
Mycoplasma contamination	Cell lines were all tested negative for mycoplasma contamination.
Commonly misidentified lines (See ICLAC register)	No commonly misidentified cell lines were used.

Animals and other organisms

Policy information about studies involving animals; ARRIVE guidelines recommended for reporting animal research

Laboratory animals	The skeletally mature New Zealand rabbits (males, age of 4 months at the time of surgery, weights ranged from 3 to 3.5 kg) were purchased from Yinhai Animal Husbandry professional cooperative (Tongxiang, China). The healthy adult Chinese Hu Sheep (males, age of 2 years old at the time of surgery, weights ranged from 52.3 to 55.4 kg) were purchased from Shanghai Jiagan Biotechnology Co., LTD (Shanghai, China).
Wild animals	This study did not involve wild animals.
Field-collected samples	This study did not involve samples collected from the field.
Ethics oversight	The rabbits experiments were approved by the Institutional Animal Care and Use Committee at Fudan University. The sheep experiments were approved by the Institutional Animal Care and Use Committee at Fudan University and the Institutional Animal Care and Use Committee of Shanghai Jiao Tong University Animal Department. All animals were housed at the animal care laboratory at the College of Pharmacy in accordance with the regulations set by the National Institutes of Health.

Note that full information on the approval of the study protocol must also be provided in the manuscript.